Improvements in spectral wave modeling in tidal inlet seas

A. J. van der Westhuysen,[1,2] A. R. van Dongeren,[1] J. Groeneweg,[1] G. Ph. van Vledder,[3,4,5] H. Peters,[6] C. Gautier,[1] and J. C. C. van Nieuwkoop[1,7]

Received 16 December 2011; revised 13 April 2012; accepted 30 May 2012; published 3 August 2012.

[1] The performance of the spectral wind wave model SWAN in tidal inlet seas was assessed on the basis of extensive wave measurements conducted in the Amelander Zeegat tidal inlet and the Dutch Eastern Wadden Sea, as well as relevant data from other inlets, lakes, estuaries and beaches. We found that the 2006 default SWAN model (version 40.51), the starting point of the investigation, performed reasonably well for measured storm conditions, but three aspects required further attention. First, over the near-horizontal tidal flats, the computed ratio of integral wave height over water depth showed an apparent upper limit using the default depth-limited wave breaking formulation and breaker parameter, resulting in an underprediction of wave heights. This problem has been largely solved using a new breaker formulation. The second aspect concerns wave-current interaction, specifically the wave age effect on waves generated in ambient current, and a proposed enhanced dissipation in negative current gradients. Third, the variance density of lower-frequency wind waves from the North Sea penetrating through the inlets into the Wadden Sea was underpredicted. This was improved by reducing the bottom friction dissipation relative to that of the default model. After a combined calibration, these improvements have resulted in a relative bias reduction in H_{m0} from −3% to −1%, in $T_{m-1,0}$ from −7% to −3%, and in T_{m01} from −6% to −2%, and consistent reductions in scatter, compared to the 2006 default model.

Citation: van der Westhuysen, A. J., A. R. van Dongeren, J. Groeneweg, G. P. van Vledder, H. Peters, C. Gautier, and J. C. C. van Nieuwkoop (2012), Improvements in spectral wave modeling in tidal inlet seas, *J. Geophys. Res.*, *117*, C00J28, doi:10.1029/2011JC007837.

1. Introduction

[2] The Dutch Wadden Sea (Figure 1) is a complex coastal system, which is enclosed by a series of barrier islands and the mainland coasts of the provinces of North Holland, Friesland and Groningen. Tidal inlets are found between the barrier islands, each featuring an ebb tidal delta, one or more main tidal channels, and a complex system of smaller channels and flats extending into the Wadden Sea interior. Some of these inlets are relatively closed (e.g., the Amelander Zeegat, Figure 1), and some are relatively open (e.g., the mouth of the Eems-Dollard estuary, Figures 1 and 2). Apart from tidal channels, the Wadden Sea interior is shallow and flat, with tidally modulated depths normally ranging between 0 m (drying) and 3 m. During extreme storms, storm surges can cause total water depths to increase by about 4 m over astronomical high water.

[3] Various types of wave models are available to simulate wave fields over coastal domains such as this. These can be broadly divided into phase-resolving (e.g., time domain) and phase-averaging (spectral) models. Considering the relatively large spatial extent of the study domain (several hundred wave lengths), phase-resolving models are currently too computationally intensive for this purpose. Spectral action balance models offer the required computational efficiency to enable practical application. However, this comes at the expense of loss of phase information and higher-order statistics, including details of the crest shape. This is arguably not critical in deep water applications, but in shallow water it necessitates a high degree of parameterization of processes such as nonlinear triad interaction and depth-induced breaking (see further discussion below).

[4] The processes which are the most important for large-scale wave transformation are included (with various degrees of parameterization) in the phase-averaged spectral wind wave model SWAN [*Booij et al.*, 1999]; see equation (1). Complex tidal seas provide a good test for this model, because a great number (if not all) of the known physical processes play a role in the wave field evolution. Despite

[1]Deltares, Delft, Netherlands.
[2]Now UCAR Visiting Scientist at NCEP, NWS, NOAA, Camp Springs, Maryland, USA.
[3]Alkyon, ARCADIS Nederland BV, Emmeloord, Netherlands.
[4]Now at BMT ARGOSS, Vollenhove, Netherlands.
[5]Environmental Fluid Mechanics, Department CiTG, Delft University of Technology, Delft, Netherlands.
[6]Rijkswaterstaat Data-ICT-Dienst, Delft, Netherlands.
[7]Now at College of Engineering, Mathematics and Physical Sciences, University of Exeter, Cornwall, UK.

Corresponding author: A. J. van der Westhuysen, UCAR Visiting Scientist at NCEP, NWS, NOAA, 5200 Auth Rd, Camp Springs, MD 20746, USA. (andre.vanderwesthuysen@noaa.gov)

0148-0227/12/2011JC007837

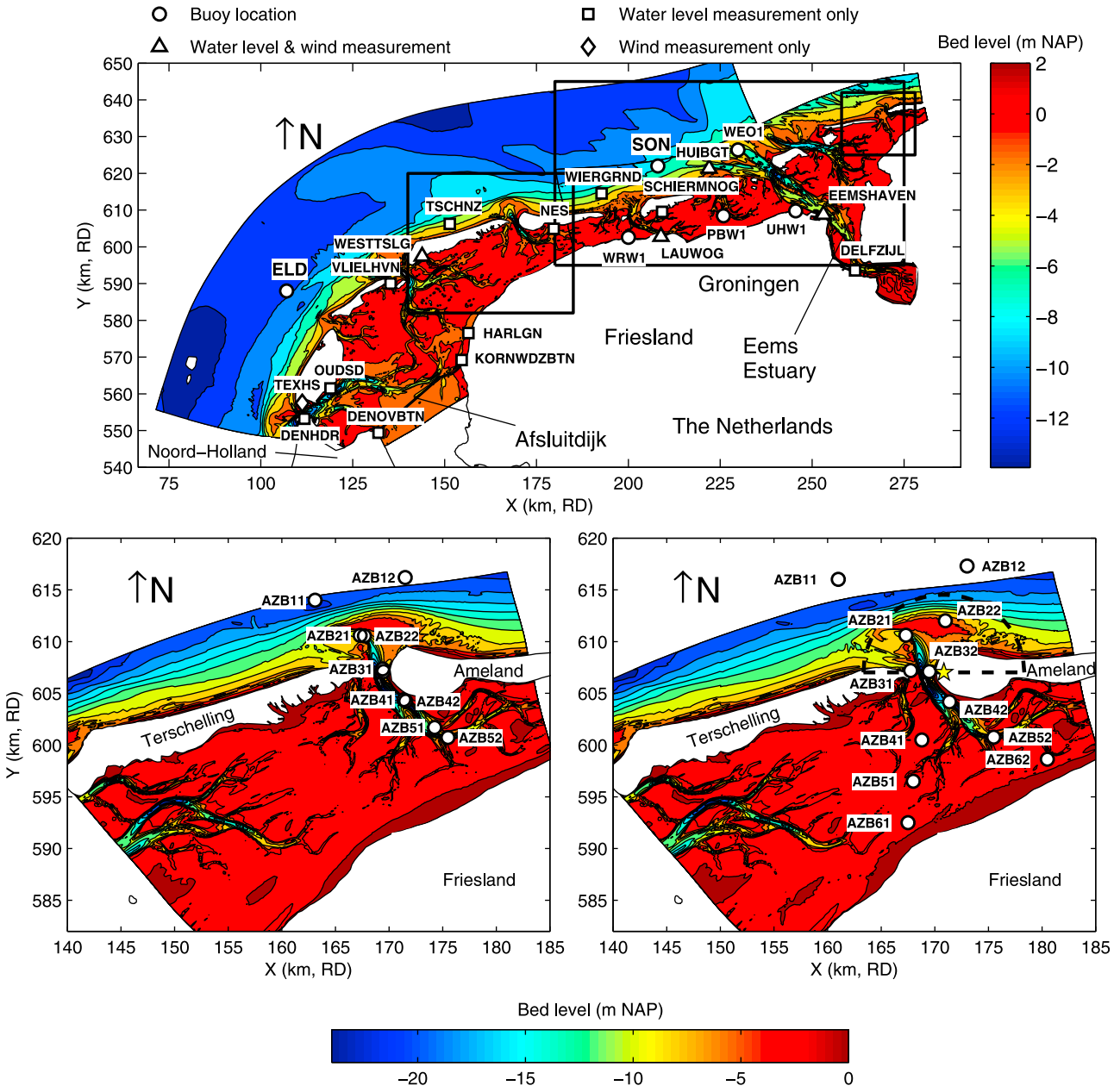

Figure 1. (top) Bathymetry of the Dutch Wadden Sea and observation locations. The boxes indicate detail areas shown in the remaining panels and Figures 2 and 3. (bottom) Bathymetry of the Amelander Zeegat region in the Dutch Wadden Sea, including the locations of the wave buoys (circles), in the configuration of 2003–2006 (bottom left) and 2007–present (bottom right). Included are the location (star) and range (dashed lines) of the X-band radar deployed in 2010. Bed levels are given in m below NAP (Dutch leveling datum). Projection in Dutch Rijksdriehoek (RD) system.

promising overall results using SWAN, *Ris et al.* [1999] showed some significant discrepancies between model results and (relatively sparse) observations in the Friesche Zeegat (Dutch Wadden Sea, Figure 1) and Norderneyer Seegat (German Wadden Sea, Figures 1 and 3) tidal inlets. Similarly, *Kaiser and Niemeyer* [2001] showed that SWAN performs reasonably well, but that it underestimates the penetration of lower-frequency wind sea from the North Sea into the Norderneyer Seegat inlet, implying that further testing and development are required.

[5] In compliance with the Dutch Flood Defenses Act ('Waterwet, 2009'), the safety of these Dutch primary sea defenses must be assessed every six years for the required level of protection. The procedure is to derive normative metocean conditions at the locations of offshore observational buoys, and transform these using stationary SWAN simulations to obtain wave conditions near the sea defenses. This procedure has hitherto been applied to the entire Dutch coast except the Wadden Sea. Up to 2002, the model could

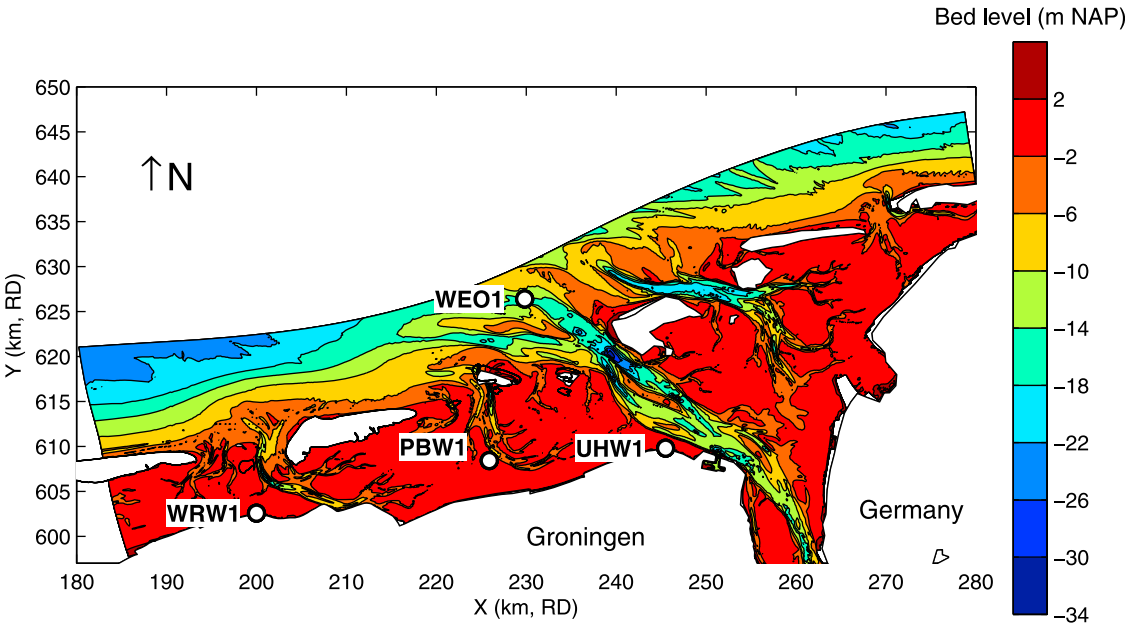

Figure 2. Bathymetry of the Dutch Eastern Wadden Sea, featuring the mouth of the Eems-Dollard Estuary. Included are the locations of the wave buoys (circles).

not be assessed thoroughly in this region, since very little wave data were available here.

[6] Therefore, the Dutch Public Works Department (Rijkswaterstaat) started the SBW (Strength and Loads of Water Defenses) programme. Within this framework, an extensive measurement campaign was set up in the Amelander Zeegat tidal inlet in 2003, and later extended to the Eastern Dutch Wadden Sea, to fill the above mentioned need for wave data [*Zijderveld and Peters*, 2008]. In 2006, a research programme was initiated, with one of its aims to assess and possibly improve the performance of the wave transformation model SWAN in the Dutch Wadden Sea under the 1/4000 per year normative condition for which the

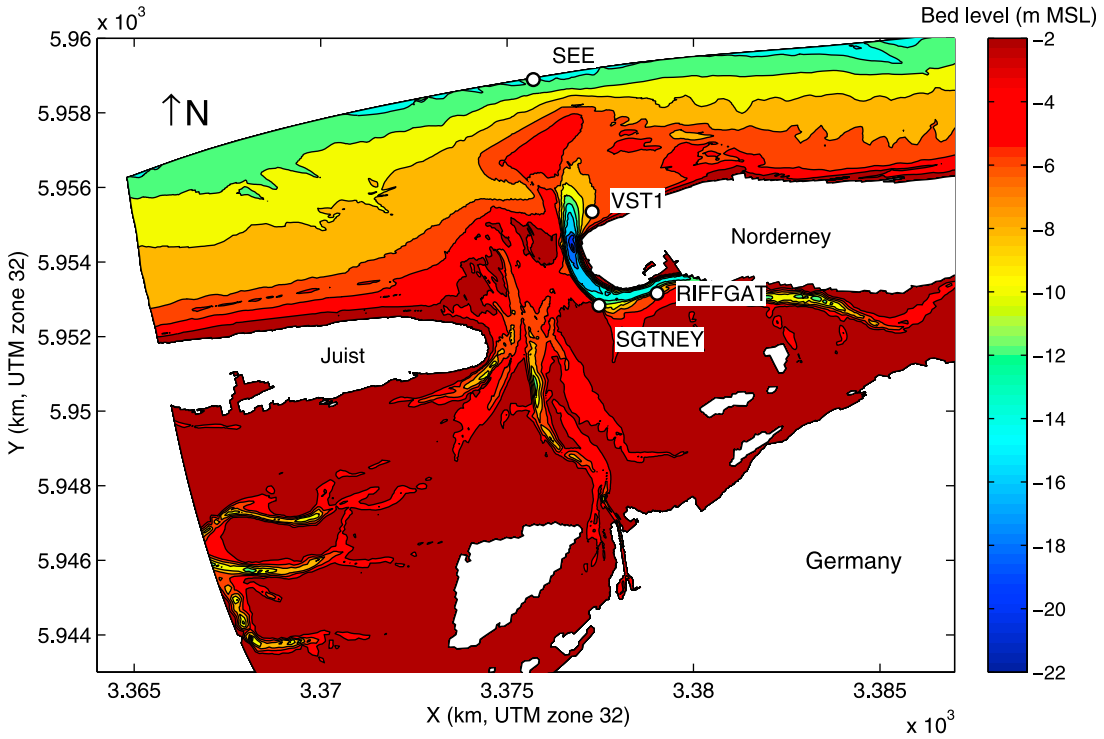

Figure 3. Bathymetry of the Norderneyer Seegat, German Wadden Sea, including the locations of the wave buoys (circles). Bed level relative to MSL. Projection in UTM zone 32.

sea defenses are assessed, with a focus on the shallow water processes.

[7] The objective of this paper is to demonstrate the main results of this project and identify remaining research topics. It focuses on three issues that required improvement based on the performance of the default model. First, over the tidal flats the computed ratio of significant wave height over water depth showed an apparent upper limit—under-estimating observations—using the conventional *Battjes and Janssen* [1978] depth-limited wave breaking formulation, with the default value of the breaker parameter γ. Second, two processes related to wave-current interaction required attention, namely the so-called wave age effect on waves generated in ambient current, and enhanced dissipation due to wave steepening in negative current gradients. Finally, the energy levels of low-frequency wind sea components from the North Sea were underestimated as they penetrated into the Dutch Wadden Sea. Model improvements are proposed for all these issues. The resulting model is calibrated and the predictive performance of the proposed model is subsequently demonstrated.

[8] The paper is structured as follows: first, section 2 describes the observational program and related data sets. Section 3 presents the wave action balance equation, the 2006 default model version and performance assessment metrics. Section 4 presents the model innovations contained in the proposed model, and sections 5 and 6 present the combined calibration of these model innovations and their subsequent validation. Sections 7 and 8 close the paper with a discussion and conclusions, respectively. Appendix A provides details of the model formulations proposed in this study.

2. Observations

2.1. Permanent Monitoring Network

[9] The permanent metocean monitoring network in and around the Wadden Sea features wave, water level and wind observation stations. Wave monitoring in the Dutch Wadden Sea region includes data recorded by Waverider buoys stationed at Eierlandse Gat (ELD) and Schiermonnikoog Noord (SON), just offshore of the barrier islands at a depth of −26 m NAP and −20 m NAP (Dutch Leveling Datum) respectively (Figure 1). Observations from these buoys are available from 1979 onwards, and are used for deriving the long-term wave statistics in the offshore.

[10] Water levels (tide and surge) are monitored at a large number of stations in the Dutch Wadden Sea area, both offshore and inside the barrier islands (Figure 1). Winds are monitored at several locations as part of the monitoring network of the Royal Netherlands Meteorological Institute (KNMI). Except for the Huibertgat (indicated as HUIBGT), all these stations are situated on land, and may not be representative for conditions on open water.

2.2. SBW Observational Campaign

[11] The observational campaign within the SBW project started in 2003. The wave measurement component presently employs more than 20 wave buoys (directional and non-directional Waveriders). The initial focus of the campaign was to assess the amount of wave penetration from the North Sea through the tidal inlets, in part to evaluate the concerns of wave penetration raised by *Kaiser and Niemeyer* [2001]. The Amelander Zeegat (Figure 1) was selected as a typical, relatively shielded inlet. Initially a single transect (2003–2006, Figure 1, bottom left), and subsequently a double transect (2007–present, Figure 1, bottom right) of wave buoys was laid out through the inlet, covering the ebb tidal shoal, tidal channels and the shoals inside the Wadden Sea. From 2010, these in-situ observations have been complemented by an X-band radar deployed on the light house of Ameland, with a range of 7.5 km (half plane) covering the inlet and out to the ebb tidal delta (Figure 1, bottom right). Using commercial analysis software (www.seadarq.com), fields of wave direction and surface current can be derived from these radar observations.

[12] The Eastern Dutch Wadden Sea region, featuring the mouth of the Eems-Dollard estuary, is situated north of the province Groningen in the Netherlands (Figures 1 and 2). The inlets in this region do not have such pronounced ebb tidal deltas as the Amelander Zeegat, and thus are more exposed to waves from the North Sea. Four directional Waverider buoys were deployed in this region during the period 2006–2007: Westereems Oost (WEO1), Pieterburenwad (PBW1), Wierumerwad (WRW1) and Uithuizerwad (UHW1).

[13] These observations, together with the wave, water level and wind monitoring data (section 2.1), form an extensive data set for the calibration and validation of wave and hydrodynamic models. However, since current data was not collected, water level and current fields for the simulations presented here were computed using hydrodynamic models WAQUA and Delft3D [*Stelling*, 1983], in 2D depth-averaged mode, calibrated to the observed water levels. Also, since the wind stations discussed in section 2.1 were mostly on land, the spatially varying wind-forcing was computed using the HIRLAM model (HIgh Resolution Limited Area Model) [*Undén et al.*, 2002]. However, due to the limited spatial extent of the field cases, uniform wind fields (spatial averages of these HIRLAM results over the Wadden Sea domain) were applied in the simulations.

[14] Due also to the limited spatial extent of the Dutch Wadden Sea, and the typical wave energy travel times through the domain, wave conditions in a single inlet system are approximately stationary. Initial comparisons between nonstationary and stationary SWAN simulations showed that differences were the largest in the tidal channels, with local differences of up to 10% in significant wave height and 5% in mean period. However, in the Wadden Sea interior, and moving toward the sea defenses at the mainland coast, the differences reduce to the order of 1–2% (not shown). For this reason, stationary simulation was applied in the results presented here. Tables 1 and 2 present a selection of stationary cases in the Amelander Zeegat and the Eastern Dutch Wadden Sea for hindcasting, taken from storm events recorded during the course of the measurement campaign. These stationary cases were selected to capture significant phases during an event, such as flood, ebb and high tide. The table summarizes the prevailing conditions during each case, and indicates for which physical process the case was selected.

2.3. Other Data Sets Used

[15] Further related data sets of the Norderneyer Seegat (Germany), the Eastern Scheldt, Lake IJssel and Lake Sloten

Table 1. Selection of Stationary Cases Recorded in the Amelander Zeegat During the Period 2004–2007[a]

Date and Time (UTC)	U_{10} (m/s)	U_{dir} (°N)	Water Level (m NAP)	U_{max} (m/s)	Tidal Phase	Significant Physical Process
08/02/2004, 20:00	13.5	314	1.0	2.3	flood	wp,wci
08/02/2004, 22:30	16.6	325	2.6	0.9	high w	wp,wci
09/02/2004, 01:30	16.3	328	1.8	1.7	ebb	wp,wci
16/12/2005, 10:00	20.0	277	1.0	2.0	flood	wp,wci
16/12/2005, 23:30	15.9	331	2.3	1.0	ebb	wp,wci
17/12/2005, 10:30	15.4	339	2.0	0.5	high w	wp,wci
11/01/2007, 13:00	19.5	228	1.0	0.7	high w	fdg
11/01/2007, 22:00	17.9	275	0.9	0.6	flood	fdg
11/01/2007, 22:40	18.8	279	1.3	0.7	flood	fdg
18/01/2007, 12:20	21.1	233	0.8	1.3	ebb	fdg
18/01/2007, 14:00	20.2	263	0.6	1.0	low w	fdg
18/01/2007, 17:20	20.3	267	1.4	1.1	flood	fdg
18/01/2007, 20:40	18.9	274	2.8	1.1	high w	fdg
18/03/2007, 10:00	13.8	279	1.7	0.4	high w	fdg
18/03/2007, 14:40	18.1	266	0.7	1.2	low w	wci,fdg
18/03/2007, 15:40	17.9	271	0.6	0.8	low w	fdg
18/03/2007, 17:00	17.1	268	1.2	1.1	flood	wci,fdg
18/03/2007, 19:20	16.3	268	3.0	1.3	flood	wci,fdg
09/11/2007, 04:50	17.3	322	1.2	1.3	flood	wp,wci,fdg
09/11/2007, 09:20	18.4	326	2.7	0.7	high w	wp,wci,fdg
09/11/2007, 11:00	18.5	328	1.7	1.3	ebb	wp,wci,fdg
09/11/2007, 17:20	16.1	330	1.0	0.9	flood	wp,wci,fdg
28/01/2010, 03:58	10.5	320	0.8	1.5	flood	wci,wp
28/01/2010, 06:39	8.4	315	1.7	0.1	high w	wci,wp
28/01/2010, 09:49	8.9	329	0.7	1.3	ebb	wci,wp

[a]Computed wind speed U_{10} at 10 m height and direction U_{dir} are mean values over domain. Water level given at station Nes, and maximum computed current speed U_{max} in the inlet main channel. Acronyms: 'wp' = wave penetration, 'wci' = wave-current interaction and 'fdg' = finite-depth wave growth.

(Netherlands), Duck, NC, (USA) and laboratory experiments were used to increase the observed range of wave conditions expected in the Dutch Wadden Sea. The Norderneyer Seegat is situated between the islands of Juist (to the west) and Norderney (to the east) in the German Wadden Sea (Figure 3). Several directional wave buoys were deployed in the region from which to derive the wave loads on the flood defenses of the Norderney Island. In the absence of observations, computed water level and current fields, and uniform wind-forcing, were applied. One stationary case is considered here (Table 3).

[16] Figure 4 shows the Eastern Scheldt domain, and Table 4 presents the storm characteristics of three selected stationary cases. The water level and current fields were computed using the WAQUA model. Spatially uniform wind fields were imposed, based on wind measurements at regional stations, including some representative land stations. In the hindcasts presented here, the wave observations of one directional Waverider (SCHB), one non-directional Waverider (DORA) and two step gauges (BG2 and OS4) were used (Figure 4). As the Eastern Scheldt Storm Surge Barrier was open during all hindcasting events, normal tidal motion was present, and no reflections occurred off the barrier gates.

Table 2. Selection of Stationary Cases Recorded in the Eastern Dutch Wadden Sea During the Period 2006–2007[a]

Date and Time (UTC)	U_{10} (m/s)	U_{dir} (°N)	Water Level (m NAP)	U_{max} (m/s)	Tidal Phase	Significant Physical Process
09/11/2007, 06:20	17.3	326	1.9	0.7	low w	wp,fdg
09/11/2007, 07:00	19.9	326	2.3	0.8	flood	fdg
09/11/2007, 09:40	18.4	332	3.1	0.3	high w	wp,fdg
09/11/2007, 11:00	18.9	333	2.8	0.5	ebb	fdg
09/11/2007, 13:40	19.5	333	1.3	1.1	ebb	wp

[a]Computed wind speed U_{10} and direction U_{dir} are mean values over domain. Water level at station Huibertgat (HUIBGT) and maximum computed current speed U_{max} in the inlet main channel. Acronyms: 'wp' = wave penetration and 'fdg' = finite-depth wave growth.

Table 3. Selected Stationary Case Recorded in the Norderneyer Seegat[a]

Date and Time (UTC)	U_{10} (m/s)	U_{dir} (°N)	Water Level (m NN)	U_{max} (m/s)	Tidal Phase	Significant Physical Process
05/02/1999, 03:36	19.0	290	3.4	0.8	high w	wci

[a]Computed wind speed U_{10} and direction U_{dir} are mean values over domain. Water level at Riffgat (relative to German leveling datum Normal Null) and maximum computed current speed U_{max} in the inlet main channel. Acronym: 'wci' = wave-current interaction.

[17] Tables 5 and 6 present stationary cases selected from storms recorded in Lake IJssel and Lake Sloten as part of the wave monitoring network in the Dutch lakes. Lake IJssel and Lake Sloten have fairly flat beds with depths of 4–5 m and 1.7 m respectively. Wave, water level and wind data for these lakes have been collected at a number of stations; see *Bottema and van Vledder* [2009] for details. Spatial averages of these wind and water level measurements were applied uniformly over the model domain. No current fields were used in the SWAN hindcasts of these lakes, since wind-generated currents are expected to be weak, and hence wave-current interaction to be of minor importance (hence omitted in Tables 5 and 6).

[18] The processes of depth-induced breaking and nonlinear triad (three-wave) interaction were considered by including field observations taken at Duck, NC, over 6–13 October 1990 during the DELILAH experiment [*Birkemeier et al.*, 1997], as well as laboratory cases of *Battjes and Janssen* [1978] and *Boers* [1996]. These cases were used for calibration purposes; see below.

2.4. Division Into Calibration and Validation Sets

[19] After a number of model innovations are discussed in section 4, section 5 will present the combined calibration of the proposed model for a selection of new model parameters. For this purpose, the data presented above (except the January 2010 cases in the Amelander Zeegat) were divided into calibration and validation subsets, with both subsets containing cases pertaining to the aspects of model improvement investigated (Table 7).

3. Method

3.1. SWAN Governing Equations

[20] The spectral wind wave model SWAN [*Booij et al.*, 1999] computes the evolution of wave action density $N(=E/\sigma$, where E is the variance density and σ the relative radian frequency) using the action balance equation:

$$\frac{\partial N}{\partial t} + \nabla_{x,y} \cdot \left[(\vec{c}_g + \vec{U}) N \right] + \frac{\partial}{\partial \theta}(c_\theta N) + \frac{\partial}{\partial \sigma}(c_\sigma N) = \frac{S_{tot}}{\sigma} \quad (1)$$

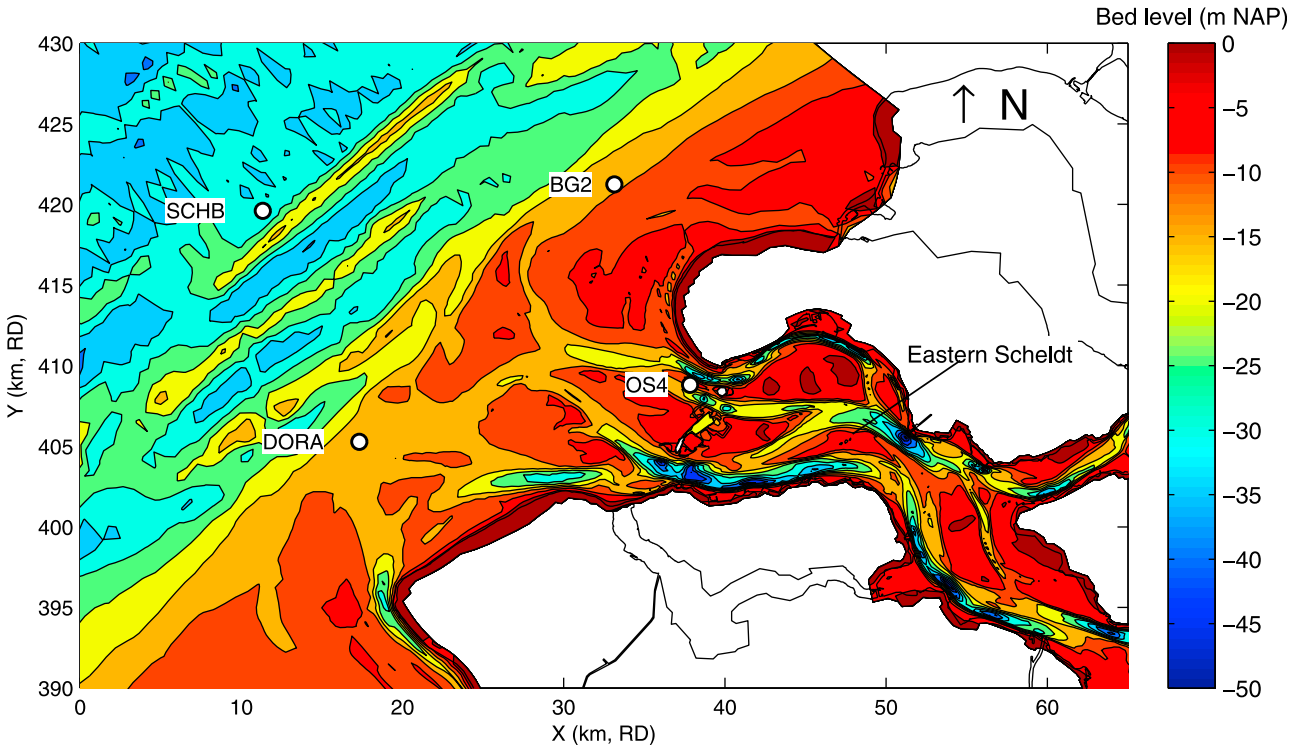

Figure 4. Bathymetry of the mouth of the Eastern Scheldt, the Netherlands, including the locations of the wave buoys and step gauges (circles). Storm Surge Barrier situated just inshore of station OS4.

with

$$S_{\mathrm{tot}} = S_{\mathrm{in}} + S_{\mathrm{wc}} + S_{\mathrm{nl4}} + S_{\mathrm{bot}} + S_{\mathrm{brk}} + S_{\mathrm{nl3}} + S_{\mathrm{wc,cur}} \qquad (2)$$

where θ is direction. The terms on the left-hand side of (1) represent, respectively, the change of wave action in time, the propagation of wave action in geographical space (with $\vec{c}_{\mathrm{g}}$ the linear intrinsic group velocity vector and $\vec{U}$ the ambient current vector), depth- and current-induced refraction (with propagation velocity c_θ in directional space) and the shifting of the relative radian frequency σ due to variations in mean current and depth (with the propagation velocity c_σ). The right-hand side of (1) represents processes that generate, dissipate or redistribute wave energy, given by (2). In deep water, three source terms are traditionally used: the transfer of energy from the wind to the waves, S_{in}; the dissipation of wave energy due to whitecapping, S_{wc}; and the nonlinear transfer of wave energy due to quadruplet (four-wave) interaction, S_{nl4}. In shallow water, dissipation due to bottom friction, S_{bot}, depth-induced breaking, S_{brk}, and triad (three-wave) nonlinear interaction, S_{nl3}, are additionally accounted for. The last source term represents the enhanced breaking dissipation of waves on a current [*van der Westhuysen*, 2012]. Due to the fact that conditions in the field cases considered here are quasi-stationary (section 2.2), all simulations are run in stationary mode, such that $\partial N/\partial t = 0$ in (1).

[21] Equation (1) is expressed in terms of phase-averaged quantities, by which the details of individual waves, for example crest shape, are lost. Information on phase couplings can be included by retaining the higher-order bispectral evolution equation during the ensemble averaging of the underlying deterministic equations [e.g., *Herbers and Burton*, 1997]. However, this becomes computationally prohibitive, and is therefore usually omitted for applications over larger domains such as the present case. As a result, the source terms in (2), especially the shallow water processes, must be

Table 4. Selection of Stationary Cases Recorded in the Eastern Scheldt[a]

Date and Time (UTC)	U_{10} (m/s)	U_{dir} (°N)	Water Level (m NAP)	U_{max} (m/s)	Tidal Phase
26/12/2001, 09:00	16.0	310	1.0	0.3	flood
26/12/2001, 12:00	13.0	315	1.5	0.5	high w
23/12/2003, 02:30	9.0	295	1.3	0.8	high w

[a]Computed wind speed U_{10} and direction U_{dir} are mean values over domain. Water level at station BG2 and maximum computed current speed U_{max}. These conditions are used for assessing wave penetration.

Table 5. Selection of Stationary Cases Recorded in Lake IJssel[a]

Date and Time (UTC)	U_{10} (m/s)	U_{dir} (°N)	Water Level (m NAP)	Significant Physical Process
02/10/1999, 03:00	15.2	215	−0.20	fdg
22/02/2002, 04:00	18.8	215	0.08	fdg
27/10/2002, 14:20	23.2	249	−0.26	fdg
08/01/2005, 13:00	19.9	246	−0.20	fdg
12/02/2005, 15:00	18.3	286	−0.39	fdg
18/01/2007, 12:00	22.4	237	0.06	fdg
18/01/2007, 19:00	23.5	267	0.10	fdg

[a]Water level represents the lake mean (Dutch: 'meerpeil') and currents were omitted. Wind speed U_{10} and direction U_{dir} are mean values over domain. Acronyms: 'fdg' = finite-depth wave growth.

Table 6. Selection of Stationary Cases Recorded in Lake Sloten[a]

Date and Time (UTC)	U_{10} (m/s)	U_{dir} (°N)	Water Level (m NAP)	Significant Physical Process
12/02/2002, 13:00	15.0	253	−0.43	fdg
26/02/2002, 14:00	20.8	243	−0.29	fdg
27/10/2002, 15:00	21.4	252	−0.45	fdg
20/03/2004, 20:00	19.4	241	−0.46	fdg
18/01/2007, 12:00	21.9	234	−0.46	fdg

[a]Water level, wind speed U_{10} and wind direction U_{dir} at station SL29. Currents were omitted. Acronyms: 'fdg' = finite-depth wave growth.

parameterized without variables that relate directly to wave phases, phase coupling or crest shape. Examples of these are the Lumped Triad Approximation (LTA) [*Eldeberky*, 1996] for triad nonlinear interactions and the bore-based model of *Battjes and Janssen* [1978] for bulk depth-induced breaking dissipation. As a result, these parameterizations may only be applicable within the data range, as discussed below.

[22] Since its introduction more than a decade ago, SWAN has been continuously developed, and improved versions have been published by Delft University of Technology, which maintains the code. It is therefore not possible to speak of a single SWAN model, but rather of model versions, including their source term and parameter settings. In this study we consider two versions, namely a default defined in section 3.2 and a proposed version given in section 5.

3.2. Default 2006 Model Formulations and Settings

[23] We define the model version 40.51, current at the start of the project in 2006, as the default version for the purpose of this study. For this version, the following default settings were applied (a selection of the expressions are presented in Appendix A):

[24] 1. Quadruplet interactions using the DIA formulation by *Hasselmann et al.* [1985], with $C_{nl4} = 3 \times 10^7$ and $\lambda = 0.25$.

[25] 2. JONSWAP formulation of *Hasselmann et al.* [1973] for bottom friction with the coefficient $C_{f,JON} = 0.067\ m^2/s^3$, as proposed by *Bouws and Komen* [1983] for fully developed wind-sea conditions in shallow water.

[26] 3. Depth-induced wave breaking according to *Battjes and Janssen* [1978], with $\alpha_{BJ} = 1.0$ and $\gamma = 0.73$.

[27] 4. Triad interactions using the LTA formulation [*Eldeberky*, 1996], with $\alpha_{EB} = 0.10$ and $f_{max,EB} = 5\ f_{m01}$ (high-frequency cut-off for the nonlinear transfer).

[28] 5. The current-induced dissipation term $S_{wc,cur}$ in (2) is not included.

[29] In addition, the following two non-default options were applied, previously shown to produce improved results (see references below):

[30] 1. Wind generation and whitecapping based on *van der Westhuysen et al.* [2007], but corrected for an underprediction of swell energy [*van der Westhuysen*, 2007]; see Appendix A1 for details.

[31] 2. The number of iterations in the stationary runs was fixed at 80 to ensure full convergence, based on the finding of *Zijlema and van der Westhuysen* [2005] that the default

Table 7. Division of Stationary Cases Into Calibration and Validation Subsets[a]

Case	Date and Time (UTC)	Calibration	Validation	Case	Date and Time (UTC)	Calibration	Validation
AZG	08/02/2004, 20:00		X	NSG	05/02/1999, 03:36		X
	08/02/2004, 22:30		X	ES	26/12/2001, 09:00		X
	09/02/2004, 01:30		X		26/12/2001, 12:00		X
	16/12/2005, 10:00		X		23/12/2003, 02:30		X
	16/12/2005, 23:30		X	LIJ	02/10/1999, 03:00		X
	17/12/2005, 10:30		X		22/02/2002, 04:00		X
	11/01/2007, 13:00		X		27/10/2002, 14:20	X	
	11/01/2007, 22:00	X			08/01/2005, 13:00		X
	11/01/2007, 22:40	X			12/02/2005, 15:00		X
	18/01/2007, 12:20		X		18/01/2007, 12:00	X	
	18/01/2007, 14:00	X			18/01/2007, 19:00	X	
	18/01/2007, 17:20		X	LSL	12/02/2002, 13:00		X
	18/03/2007, 19:20	X			26/02/2002, 14:00		X
	18/01/2007, 20:40	X			27/10/2002, 15:00		
	18/03/2007, 10:00		X		20/03/2004, 20:00		X
	18/03/2007, 14:40		X		18/01/2007, 12:00		X
	18/03/2007, 15:40	X		DELI	07/10/1990, 13:00[b]	X	
	18/03/2007, 17:00		X		09/10/1990, 10:00[b]	X	
	18/03/2007, 19:20	X			09/10/1990, 13:00[b]	X	
	09/11/2007, 04:50		X	BJ	Run 13	X	
	09/11/2007, 09:20	X			Run 15	X	
	09/11/2007, 11:00	X		BRS	Run 1C	X	
	09/11/2007, 17:20		X				
EW	09/11/2007, 06:20	X					
	09/11/2007, 07:00	X					
	09/11/2007, 09:40	X					
	09/11/2007, 11:00		X				
	09/11/2007, 13:40		X				

[a]AZG = Amelander Zeegat, EW = Eastern Wadden Sea, NSG = Norderneyer Seegat, ES = Eastern Scheldt, LIJ = Lake IJssel, LSL = Lake Sloten, DELI = DELILAH experiment, BJ = *Battjes and Janssen* [1978] and BRS = *Boers* [1996].
[b]Times in local time.

convergence criteria can lead to poorly converged results with significant error. Note that a small amount of underrelaxation has been applied. This was done to improve the iterative solution of the source terms over this complex domain, which sometimes features isolated grid points, for example behind islands. It was verified that this has no impact on the final model outcomes.

[32] 3. Default propagation schemes for stationary computation were applied. This includes the second-order upwind scheme (SORDUP) in geographic space, and an equal mix of central and first-order upwind schemes for both frequency and directional propagation.

3.3. Qualitative and Quantitative Performance Assessment

[33] In order to assess the performance of SWAN in its default and proposed forms, we computed a total of 29 stationary hindcast cases from the validation subset (Table 7) with the default SWAN version. Because there are a number of buoys per inlet, the total number of data points is 161. The computed and observed variance density spectra will be evaluated below to qualitatively identify shortcomings in the model performance. In addition, scatterplots of integral properties were made and quantitative scoring indexes were defined. These are the scatter index and relative bias scores, which were computed for the significant wave height H_{m0}, and spectral periods $T_{m-1,0}$ and T_{m01}. The error measures are defined, respectively, as:

$$SCI_{\Psi} = \frac{\sqrt{\frac{1}{n}\sum_{i=1}^{N}\left(\Psi_{SWAN}^{i} - \Psi_{obs}^{i}\right)^{2}}}{\frac{1}{n}\sum_{i=1}^{N}\Psi_{obs}^{i}} \quad (3)$$

and

$$\mathrm{Rel.bias}_{\Psi} = \frac{\sum_{i=1}^{N}\left(\Psi_{SWAN}^{i} - \Psi_{obs}^{i}\right)}{\sum_{i=1}^{N}\Psi_{obs}^{i}} \quad (4)$$

where Ψ_{obs} is the observed significant wave height $H_{m0,obs}$ or spectral periods $T_{m-1,0,obs}$ or $T_{m01,obs}$, and Ψ_{SWAN} is the corresponding modeled result $H_{m0,SWAN}$, $T_{m-1,0,SWAN}$ or $T_{m01,SWAN}$, in a sample of size N.

[34] We chose to assess the performance of the model based on these quantities because they are the most important wave parameters that are used as input in the water defense safety assessment rules. Wave direction is also used in the assessment. However, since fewer instruments were available to measure wave direction, the sample set was considered to small to include in the error statistics. The computed and observed (where available) directions are included in the wave spectra comparisons below.

4. Model Innovations

[35] Three innovations developed for improved model performance in the Dutch Wadden Sea are presented below. These are the improved modeling of depth-induced breaking in situations of finite-depth wave growth, such as found in the Wadden Sea interior (section 4.1), model development related to wave-current interaction (section 4.2), and improved modeling of wave penetration into the interior of the Wadden Sea (section 4.3).

4.1. Depth-Induced Breaking Under Finite-Depth Wave Growth Conditions

[36] The first model improvement is related to local wave growth in the finite depths of the Wadden Sea interior. Specifically, it concerns the modeling of depth-induced breaking under such conditions. From *De Waal* [2001] and *Bottema and van Vledder* [2009] it is known that wave heights are underestimated in finite-depth wave growth situations in shallow lakes by SWAN. It is to be expected that this model deficiency would also be relevant to the conditions in the Dutch Wadden Sea, since it contains extensive tidal flat areas (Figure 1) that are dominated by local wind sea.

[37] By way of illustration, Figure 5 presents wave spectra at the Amelander Zeegat buoys AZB51, AZB61 and AZB62 for the validation case 18/01/2007 at 12:20 UTC, featuring strong finite-depth growth ($gd/U_{10}^2 = 0.039$, where U_{10} is the wind measured at 10 meters height and d the depth at the buoy). The default model (dash-dotted lines) shows less wave growth compared to the measured spectra (solid with dots), yielding smaller total variance and a higher peak frequency, reflecting the results in the Dutch lakes mentioned above. Note that wave direction was not observed at these measurement buoys. As discussed in *van der Westhuysen* [2010], this underestimation is due to a balance in the model between local wind wave growth and depth-induced breaking modeled using *Battjes and Janssen* [1978] with the default value of the breaking parameter. The remaining model variants in Figure 5 are discussed in section 6.

[38] The observations of the Amelander Zeegat, Lake IJssel and Lake Sloten (calibration plus validation subsets) are replotted in Figure 6 (left) in terms of H_{m0}/d versus the non-dimensional depth gd/U_{10}^2. Added to these are data from Lake George, a shallow lake in Australia [*Young and Verhagen*, 1996]. Lake Sloten and Lake IJssel can be identified as two distinct populations, while the Amelander Zeegat and Lake George data both cover the parameter range of the former two populations. This last point is an important finding since it allows lake data to be used for the assessment of the wave model for the finite-depth wave growth aspect in the Wadden Sea (and vice versa). The reason for the two distinct populations for Lake IJssel and Lake Sloten is unknown at this point, but the hypothesis is that it has a relation with ripple heights in the bed in either lake which do not enter the scaling. Figure 6 (right) presents this data in terms of nondimensional energy g^2E/U_{10}^4 versus nondimensional depth gd/U_{10}^2. Comparing the observed data with the empirical finite-depth wave growth limit proposed by *Young and Babanin* [2006, equation (10)], derived from Lake George data, shows that the latter underestimates the Dutch Wadden Sea and Lake IJssel data. It is therefore not advisable to calibrate SWAN to this empirical relation, but rather to consider the individual field cases themselves.

[39] In previous unpublished studies for Lake IJssel and Lake Sloten (e.g., *De Waal et al.* [1997], using HISWA [*Holthuijsen et al.*, 1989]), either the value of the α_{BJ} parameter in *Battjes and Janssen* [1978] was decreased from unity, or the value of the breaking index γ parameter was increased from the default value of $\gamma = 0.73$ to about $\gamma = 0.8$–0.9 to obtain accurate predictions. In other words, using the default breaking parameterization, a good model-data

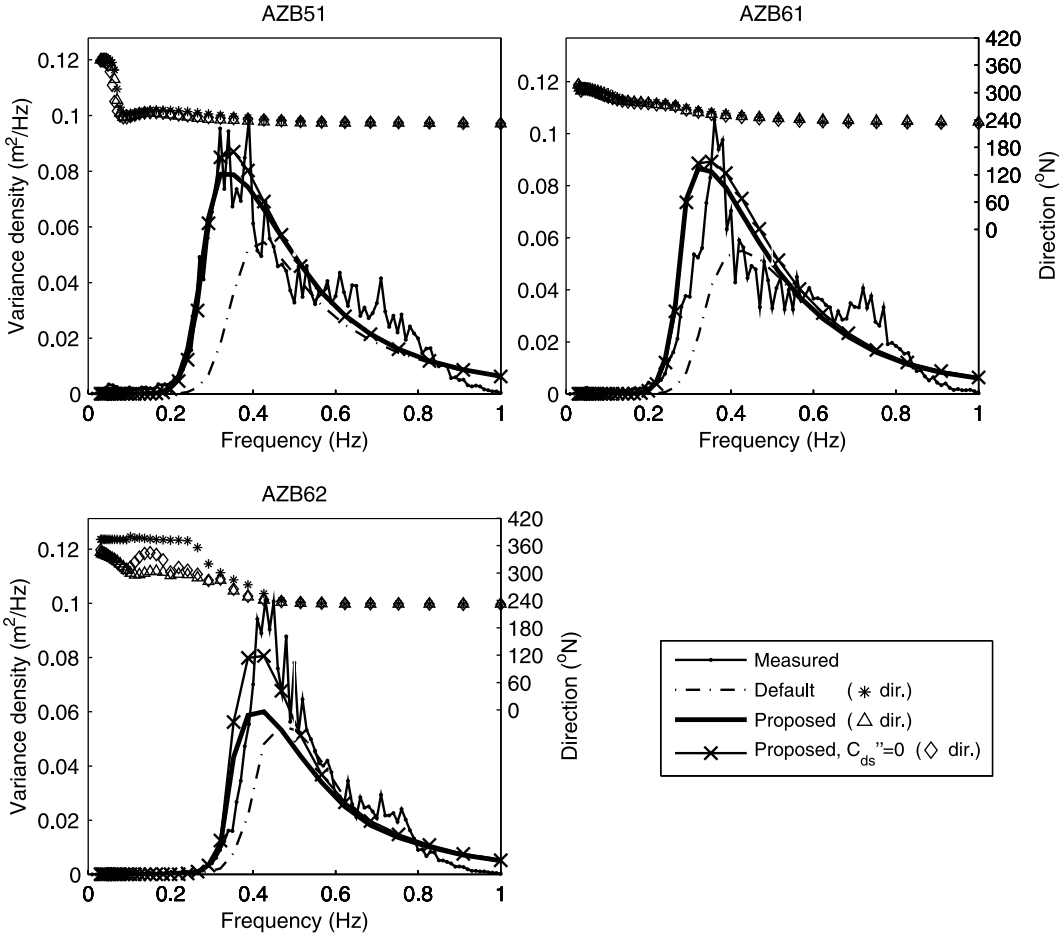

Figure 5. Variance density spectra of a finite-depth growth case in the Amelander Zeegat (18/01/2007, 12:20 UTC). Shown are observations (solid with dots), and SWAN default (dash-dot) and proposed (thick solid) model results. Also shown are intermediate results featuring the *van der Westhuysen* [2009] breaker model, but without enhanced dissipation on current gradients (solid with crosses).

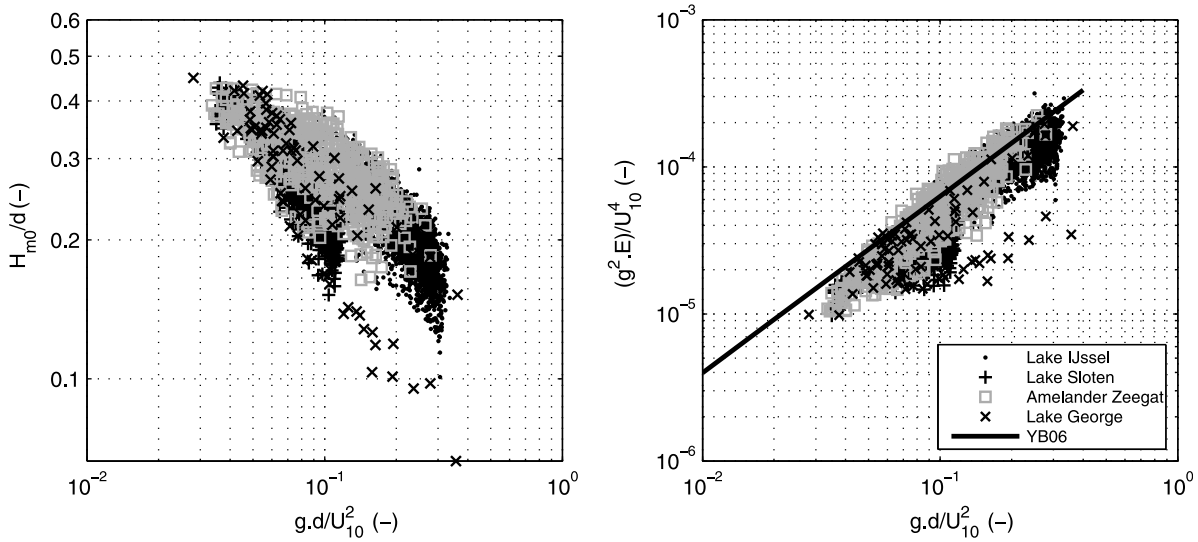

Figure 6. Finite-depth growth curves. (left) Nondimensional ratio H_{m0}/d versus nondimensional depth (gd/U_{10}^2) for the finite-depth wave growth data set. (right) Nondimensional energy g^2E/U_{10}^4 versus nondimensional depth (gd/U_{10}^2) for the finite-depth wave growth data set and equation (10) of *Young and Babanin* [2006], labeled YB06.

match could only be obtained after tuning of a parameter value which is then not universal anymore, which is an undesirable situation.

[40] To address this issue, a number of existing parameterizations of the breaker index γ were investigated [e.g., *Battjes and Stive*, 1985; *Nelson*, 1994; *Ruessink et al.*, 2003; *Apotsos et al.*, 2008]. These parameterizations are all formulated for situations of sloping beaches or flat-topped reefs that are open to the deep sea. *Apotsos et al.* [2008], for example, is defined in terms of an offshore wave height, which is not defined in an enclosed coastal basin. As such, they do not perform well in situations of finite-depth wave growth in enclosed water, with the exception of *Ruessink et al.* [2003], who present an empirical relation without a physics-based theory. *Van der Westhuysen* [2009, 2010] found that the optimal value of γ, based on minimizing the bias and scatter index, can be divided into two populations: one for sloping beaches (waves generated in deep water, subsequently breaking on a beach) and one for finite-depth wave growth (near-horizontal bed) cases. For both wave height and wave period, the sloping beach cases show a minimum error for γ values around 0.6–0.8, i.e., around the commonly used default of $\gamma = 0.73$, whereas for the cases with finite depth growth over nearly horizontal beds the errors are monotonically decreasing with increasing γ. This indicates that the optimal result is reached when the *Battjes and Janssen* [1978] model parameter γ is set such that depth-limited wave breaking is effectively turned off. Thus, in the equilibrium balance, depth-limited breaking has a smaller dissipation contribution in the case of nearly horizontal beds under local wind forcing than in the case of sloping beaches. Here the input by the wind is balanced by the dissipation through whitecapping and bottom friction.

[41] *Van der Westhuysen* [2010] proposes to modify the breaker formulation by *Thornton and Guza* [1983], itself a modification of *Battjes and Janssen*'s [1978] formulation, to provide accurate results in finite-depth wave growth conditions while retaining good performance over sloping beaches (see Appendix A2). *Van der Westhuysen* [2010] shows that the fraction of breaking waves in this expression can be expressed as a power law of the biphase (β) of the self-interactions of the spectral peak, which, along with the skewness and asymmetry, is a measure of the shallow water nonlinearity of the waves. As waves propagate from deeper water (where they are approximately sinusoidal) to intermediate depth, they typically become more 'peaked' or skewed, but symmetrical ($\beta = 0$), and in shallow water they have a saw tooth shape and they become asymmetric ($\beta \rightarrow -\pi/2$) and break. Because SWAN is not a nonlinear phase-resolving model, it cannot compute the biphase of the waves. However, *Doering and Bowen* [1995] and *Eldeberky* [1996] related the biphase to the Ursell number, which can be computed by a phase-averaged spectral model such as SWAN, so that the problem can be closed.

[42] The model equations used here are given in *van der Westhuysen* [2009], as given in Appendix A2). These expressions have the tunable parameters B (proportionality coefficient), β_{ref} (biphase at which all waves are broken), ν (fitting parameter for the relationship between the fraction of breakers and β, weakly dependent on the wave steepness) and an average steepness $\tilde{S}_{\mathrm{loc}}$. The parameters β, ν and $\tilde{S}_{\mathrm{loc}}$ have been calibrated on the basis of breaker fraction observations of *Boers* [1996], and subsequently the proportionality coefficient B was calibrated [*van der Westhuysen*, 2009]. In section 5, the coefficient B is recalibrated together with the parameters of the remaining model innovations described below.

4.2. Wave-Current Interaction

[43] The second area of model improvement concerns two aspects related to wave-current interaction. The first is the influence of currents on the wave age, and the second is enhanced dissipation due to wave steepening in negative current gradients.

4.2.1. Wave Age Effect

[44] As described in section 1, *Kaiser and Niemeyer* [2001] reported that SWAN underestimated the wave conditions at the lee side of Norderney island at the RIFFGAT station, a validation case in the present study (Figure 3). This is reproduced in Figure 7 (bottom right panel), which shows the model as run by *Kaiser and Niemeyer* [2001] (dashed line) to underpredict the observations (solid with dots), even though the wave directions are accurate. A part of the reason is that *Kaiser and Niemeyer* [2001] used the default convergence criteria (at that time), which were rather lenient, resulting in only 15 iterations before run termination. Applying 80 iterations is more computationally intensive, but the results are now converged — in this case with higher energy levels in the wind sea spectrum at all buoys (Figure 7, dotted line).

[45] The remaining model-data disagreement at RIFFGAT can be explained by including residual tidal and wind-driven currents. Since the selected stationary case was at astronomical slack tide, *Kaiser and Niemeyer* [2001] did not take the currents into account. However, under these storm conditions, a significant wind-driven circulation current was present. The modeled current field [*Herman et al.*, 2006] (not shown) suggests that currents ran across the inlet from southwest to northeast toward Norderney and turned in a counterclockwise fashion close to the island, where the flow was directed northwesterly, jetting out of the inlet.

[46] The results using the default model including currents and increased number of iterations show a marked improvement at the RIFFGAT station (dash-dotted line, Figure 7, bottom right). The spectrum now displays enhanced wind wave growth, with a lower peak frequency and greater total variance. This is because, in applying this current field, the local waves, driven by winds from the northwest, experience a mostly opposing current before they reach RIFFGAT, which alter (in this case decreasing) their effective wave age to [e.g., *Haus*, 2007]:

$$\frac{\vec{U} + \vec{c}_{\mathrm{p}}}{\vec{u}_{*}} \tag{5}$$

where $\vec{U}$ is the current velocity vector, $\vec{c}_{\mathrm{p}}$ is the relative (intrinsic) wave phase velocity vector and $\vec{u}_{*}$ is the wind friction velocity vector. Hence, the wind is effectively blowing relatively harder over the wave field, causing enhanced wave growth. Note that the effect on the spectral

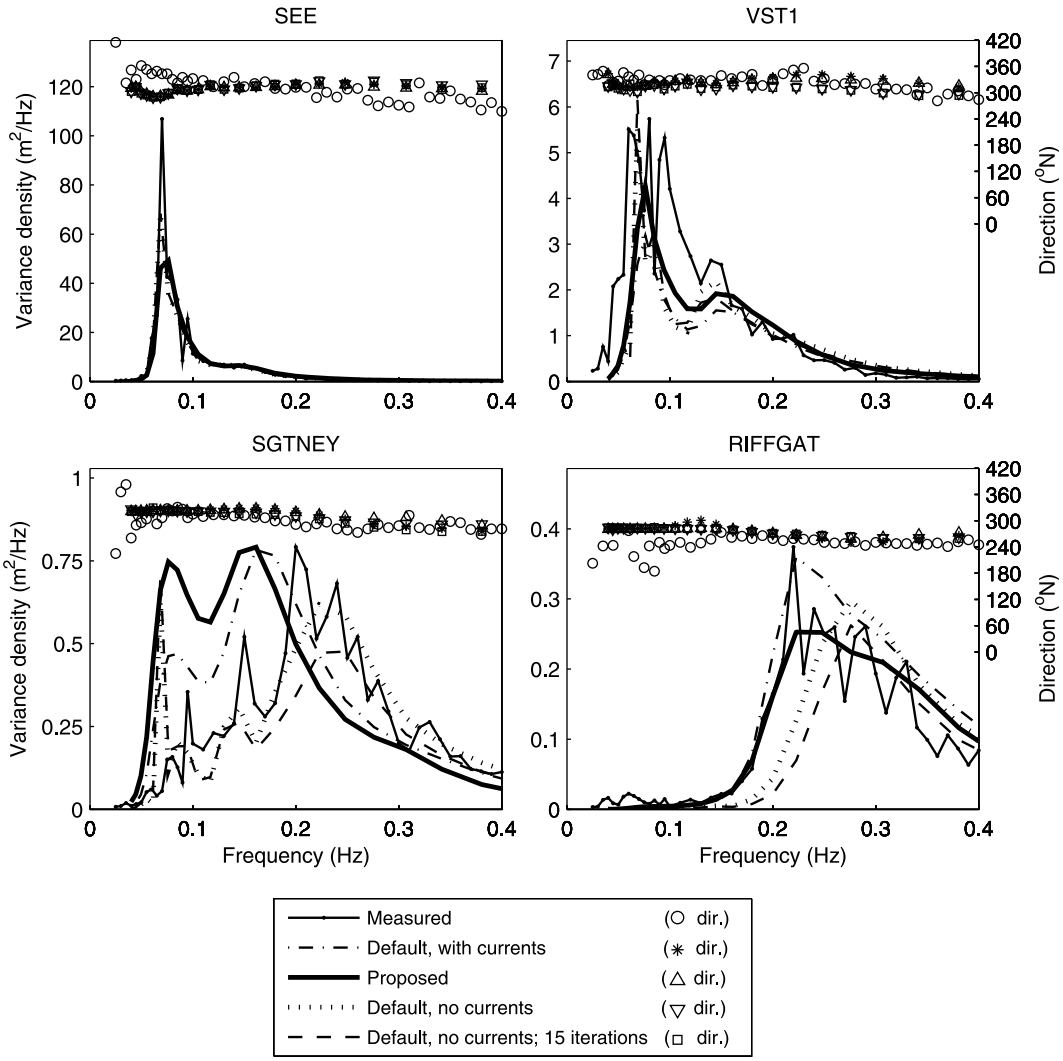

Figure 7. Variance density spectra of a wave-current interaction field case in the Norderneyer Seegat (05/02/1999, 03:36 UTC), including observations (solid with dots) and SWAN default (dash-dot) and proposed results (thick solid). Also shown are default model results without currents (dotted) and with 15 iterations (dashed). Note the difference in scale between the results at SEE and VST1, and those at SGTNEY and RIFFGAT.

mean period $T_{m-1,0}$ is opposite to what one would expect from a Doppler-shift in an opposing current without wind, represented by the fourth term on the LHS of (1).

[47] Regarding the remaining buoys around the inlet, Figure 7 shows that the application of currents (dash-dotted lines) has a small relative effect at VST1. By comparison, at SGTNEY the currents result in stronger wind sea growth, as found at RIFFGAT. However, here the wave model results featuring currents are at variance with the observed spectrum. This is likely due to the buoy location in strongly turning currents and highly varying bathymetry on the channel edge. Considering some freedom of movement of this tethered buoy over this variable region, the observations may not be representative. The remaining model variant is discussed in section 6.

4.2.2. Enhanced Dissipation on Current Gradients

[48] The second aspect of wave-current interaction addressed is the effect of current gradients on the dissipation of wave energy. *Ris and Holthuijsen* [1996] showed that wave heights can be overestimated in near-blocking, opposing current increasing in the downwave direction (a negative gradient). Similar, although less extreme, conditions exist in the tidal inlets of the Wadden Sea (maximum opposing relative current speeds of $U/c_{g,peak} = 0.4$), where H_{m0} was found to be generally overestimated by the default model in the main channel of the Amelander Zeegat.

[49] Figure 8 presents frequency spectra at the wave buoys AZB32 and AZB42 in the Amelander Zeegat for two validation cases from Table 7, one during ebb (opposing current) and one during flood (following current). Figure 8 (top row) shows that the default model overestimates the observed variance density for the opposing current case 18/03/2007 at 14:40 UTC. This occurs even while the modeled and observed wave directions are in agreement for the frequency range with significant variance, suggesting that the inaccuracy is not due to directional effects. Figure 8 (bottom row) shows that for the following current case 18/03/2007 at 17:00 UTC the default model overestimates the total variance somewhat

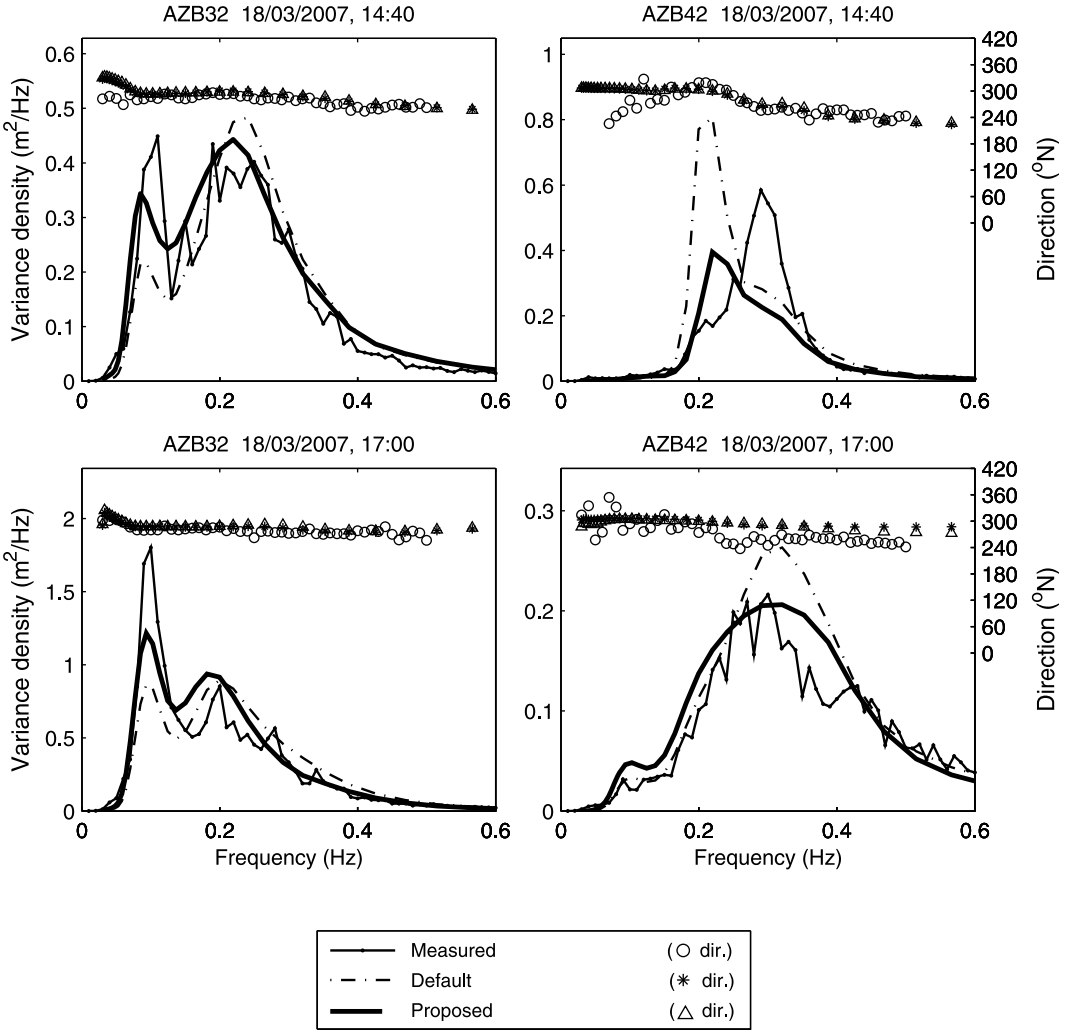

Figure 8. Variance density spectra of wave-current interaction cases in the Amelander Zeegat. Shown are observations (solid with dots) and default (dash-dot) and proposed model results (thick solid), for (top) two locations during ebb and (bottom) two locations during flood.

for AZB42 and underestimates it at the low-frequency peak for AZB32. The modeled and observed wave directions are again in agreement for the frequency range with significant variance, except at AZB42 (bottom right-hand panel). The remaining model variant is discussed in section 6.

[50] Conventional whitecapping formulations, such as that of *van der Westhuysen et al.* [2007] are typically developed and calibrated under conditions where they form a balance with the processes of wind input and quadruplet wave interaction, which results in relatively weak dissipation rates. Under strong negative current gradients, even away from the blocking point, higher rates of dissipation are evidently required. *Van der Westhuysen* [2012] presents a formulation for the enhanced dissipation of waves on current (see Appendix A3), that is based on the saturation-based whitecapping expression of *van der Westhuysen et al.* [2007]. This formulation is restricted to far field (non-blocking) conditions, so that it can be applied within the context of a spectral wave model with linear kinematic equations. The proposed scaling increases the rate of whitecapping dissipation proportional to the influence of the current. In order to isolate the contribution of currents in the increased steepness and resulting breaking dissipation, the degree of dissipation in this expression is scaled with the incremental steepening of the waves due to negative current gradients, which is related to the relative Doppler shifting rate c_σ/σ per spectral component. *Van der Westhuysen* [2012] calibrated the proportionality coefficient to $C''_{ds} = 0.65$ using laboratory data. This coefficient is recalibrated along with the parameters of the remaining model innovations in section 5.

4.3. Penetration of Low-Frequency Wind Wave Energy

[51] The Amelander Zeegat (Figure 1) measurements show very little North Sea-generated wave energy penetrating into the inlet under storm conditions. Here the ebb tidal delta functions as an efficient wave dissipator, and waves which do penetrate through the inlet gorge are quickly refracted out of the channels and dissipated over the flats. However, for more exposed inlets, e.g., in the Eems-Dollard estuary (Figures 1 and 2) and the Eastern Scheldt in the southwest of the Netherlands (Figure 4), significant wave penetration is found.

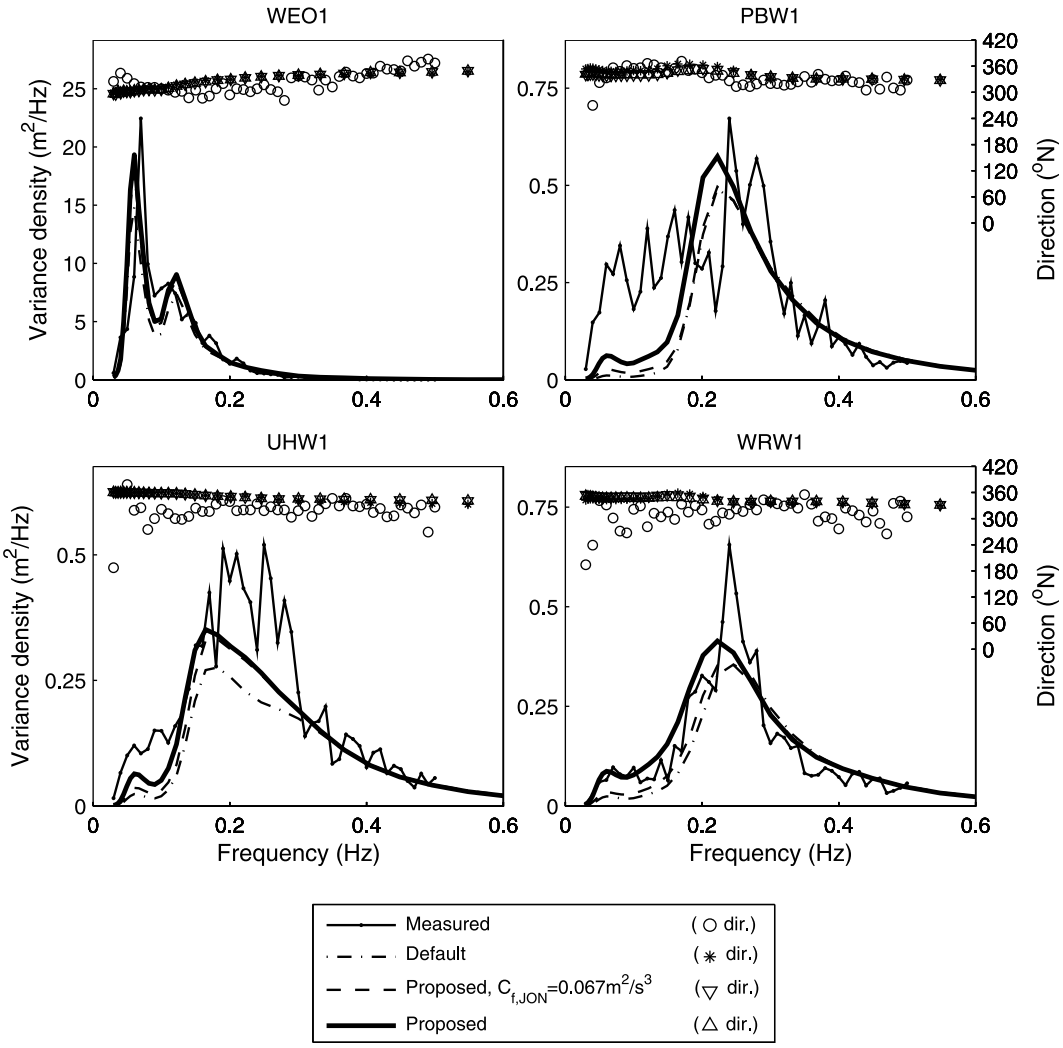

Figure 9. Variance density spectra of a North Sea wave penetration case in the Eastern Wadden Sea (09/11/2007, 11:00 UTC). Shown are observations (solid with dots), and the default (dash-dot) and proposed model results (thick solid), as well as results of proposed model, but with $C_{f,JON} = 0.067$ m^2/s^3 (dashed).

[52] The penetration of North Sea waves into the Eastern Dutch Wadden Sea was studied for the peak of the storm of 8–9 November 2007. The variance density spectra at four locations of a validation case for this site are presented in Figure 9. At the outer buoy WEO1, the model-data agreement is reasonable over the 0.05–0.2 Hz band, but at all inner buoys (WRW1, PBW1 and UHW1) the default model strongly underpredicts the variance over this frequency range (compare dash-dot and solid with dots). This occurs while the wind sea range is adequately reproduced, with the exception of UHW1. Note the change of vertical scale from the outer to the inner buoys. We verified that the low-frequency variance is not explained by lower-harmonic bound waves [*Hasselmann*, 1962; *Herbers et al.*, 1994], which are not computed by SWAN. Similar results were found for the Eastern Scheldt field cases (not shown). The remaining model variants are discussed in section 6.

[53] Analysis of the spectral evolution over the tidal channels and flats showed that changes in the 0.05–0.2 Hz band were not related to significant magnitudes of any source or sink terms (depth-induced breaking, whitecapping, etc., not shown). By elimination, this suggests that the cause of the mismatch is in the propagation terms and/or small-magnitude, but persistent, sink terms such as the bottom friction that act over large distances, both of which are discussed in more detail below.

[54] The accuracy of the wave direction modeling in the tidal inlets was investigated using data from an X-band marine radar deployed on the Ameland lighthouse overlooking the tidal inlet (Figure 1). Figure 10 presents spatial plots of simulated and radar-derived dominant wave directions in the Amelander Zeegat tidal inlet, for three tidal stages of the NW storm recorded in 28 January 2010 (Table 1). The dominant wave direction is defined as the direction of the energy bin with maximum wave energy. Up to and including the tidal inlet, this is dominated by low-frequency waves propagating from the offshore.

[55] The radar directional results (left-hand panels of Figure 10) show some typical propagation patterns, including waves entering over and around the ebb tidal shoal, refraction over the banks of the main tidal channel, wave trapping on the central shoal in the inlet and waves from the

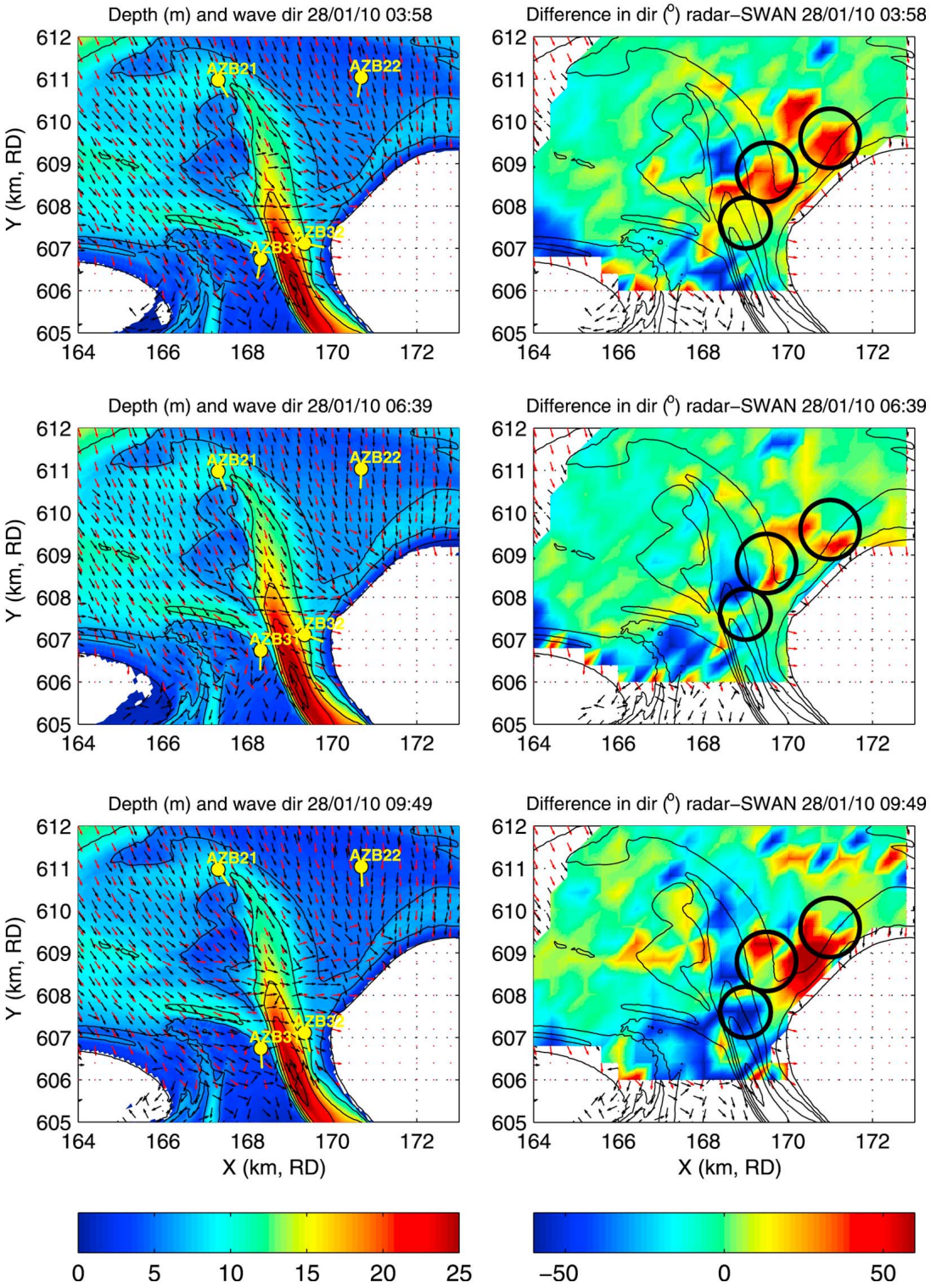

Figure 10. Comparison between dominant wave direction of SWAN and that derived from X-band radar. Results for three tidal stages during the storm of 28/01/2010: (top) flood, (middle) slack and (bottom) ebb. (left) Wave direction vectors (black = radar; red = SWAN) and depth. (right) Wave direction vectors and contour field of difference between radar-derived and SWAN dominant wave directions (nautical convention). Positive values indicate that radar results are from a more northerly direction.

west crossing over the main tidal channel toward the head of Ameland. These features are generally reproduced well by SWAN, and agree fairly well locally with the peak directions of the buoy observations (yellow dots with lines indicating wave direction). The right-hand panels show that the differences between the model results and observations are relatively small over the majority of the observed region. Some local discrepancies can be found (indicated by the black circles), in particular at locations with crossing seas. These areas are fairly consistent, although errors are somewhat greater during flood and ebb than when currents are weak (high tide). Note also that at some (random) locations, the radar wave direction is erroneously aliased by 180°, causing rather large differences in isolated areas. These have not been corrected here. These results suggest that SWAN, utilizing only depth- and current-induced refraction (no diffraction) adequately models wave propagation over complex inlets.

[56] With respect to persistent small-magnitude sink terms, the bottom friction formulation of *Hasselmann et al.* [1973] (see Appendix A4), has a proportionality coefficient with two default values in SWAN, given by *Booij et al.* [1999]. The first of these values was derived for swell conditions observed during the JONSWAP experiment [*Hasselmann et al.*, 1973] which yielded a value $C_{\mathrm{f,JON}} = 0.038\ \mathrm{m^2/s^3}$. For fully developed wind-sea conditions in shallow water a second value of $C_{\mathrm{f,JON}} = 0.067\ \mathrm{m^2/s^3}$ was found by *Bouws and Komen* [1983]. However, a re-analysis by *Zijlema et al.* [2012] reveals some inconsistencies in the determination of the friction coefficient for wind seas. Instead, they propose a setting of $C_{\mathrm{f,JON}} = 0.038\ \mathrm{m^2/s^3}$ for both swell and wind sea. Considering this uncertainty, this parameter is included in the overall calibration described in section 5.

5. Combined Calibration

[57] Sections 4.1–4.3 discussed model innovations proposed during the course of this project, which were calibrated and verified individually. This section presents the combined calibration of these expressions, to arrive at parameter settings suitable for a wide range of conditions in tidal inlet seas.

[58] The following parameters of the expressions discussed above were included in the calibration: B (depth-induced breaking), C''_{ds} (enhanced current-induced whitecapping) and $C_{\mathrm{f,JON}}$ (bottom friction). Considering the local balance that develops between depth-induced breaking and triad interactions in the surf zone [e.g., *Herbers et al.*, 2000], the proportionality coefficient of the LTA, α_{EB}, was also included in this calibration, with $f_{\mathrm{max,EB}} = 2.5\ f_{\mathrm{m01}}$ (see Appendix A5). The coefficient of the enhanced current-induced whitecapping expression was calibrated separately, since this was based on observations at the Amelander Zeegat channel buoys AZB32, AZB42 and AZB52, unlike the buoys in shallower water used for calibrating the remaining processes. A value of $C''_{\mathrm{ds}} = 0.80$ was found. It is noted that the expression was found to be insensitive to values of this coefficient over the range 0.65–0.80, so that the results are essentially similar to those using the calibration setting of $C''_{\mathrm{ds}} = 0.65$, found by *van der Westhuysen* [2012] on the basis of laboratory cases.

[59] The calibration of B, α_{EB} and $C_{\mathrm{f,JON}}$ was performed using a system based on OpenDA [*Weerts et al.*, 2010] (see also www.openda.org), a generic software environment for operational data assimilation, model uncertainty analysis and calibration. The calibration algorithm selected was the Does not Use Derivatives (DUD) method [*Ralston and Jennrich*, 1978], applied with soft constraints to prevent drifting from physically acceptable values. The Goodness of Fit (GoF) function used was based on H_{m0} and $T_{\mathrm{m-1,0}}$, being the output variables of most interest here:

$$GoF = \frac{1}{2}\sum_{i=1}^{N} W^i_{H_{\mathrm{m0}}}\left[\left(H^i_{\mathrm{m0,obs}} - H^i_{\mathrm{m0,SWAN}}\right)^2 / \left(\sigma^i_{\mathrm{obs}} H^i_{\mathrm{m0,obs}}\right)^2\right] + \frac{1}{2}\sum_{i=1}^{N} W^i_{T_{\mathrm{m-1,0}}}\left[\left(T^i_{\mathrm{m-1,0,obs}} - T^i_{\mathrm{m-1,0,SWAN}}\right)^2 / \left(\sigma^i_{\mathrm{obs}} T^i_{\mathrm{m-1,0,obs}}\right)^2\right] \quad (6)$$

in which N is the number of calibration data points (summed over all cases), $W^i_{H_{\mathrm{m0}}}$ and $W^i_{T_{\mathrm{m-1,0}}}$ are weighting functions, both set equal to 1, and σ^i_{obs} is the standard deviation of the observed parameter (H_{m0} or $T_{\mathrm{m-1,0}}$) at location i, accounting for the uncertainty or quality of the observations. Here σ^i_{obs} was used to weight the contributions of the various data sets. First, the 44 observations of the Amelander Zeegat subset were estimated to each have $\sigma^i_{\mathrm{obs}} = 0.10$. Then each of the remaining field and laboratory subsets were assigned values of σ^i_{obs} such that they would have the same weight as the Amelander Zeegat subset. Subsequently the weight of the Lake IJssel site was halved and that of the Amelander Zeegat doubled, to reflect their relative importance to the calibration. This resulted in the following values (subscript indicating data set): $\sigma^i_{\mathrm{obs,AZG}} = 0.071$, $\sigma^i_{\mathrm{obs,EW}} = 0.037$, $\sigma^i_{\mathrm{obs,LIJ}} = 0.037$, $\sigma^i_{\mathrm{obs,DELI}} = 0.069$ and $\sigma^i_{\mathrm{obs,lab}} = 0.081$. The objective of the calibration is to iteratively minimize (6). The tolerances for this process were set at 0.001 (absolute) and 0.01% (relative), which are values specific to the GoF as defined here. During the iterative calibration process, the parameter values defined above are varied as follows: B with a normal distribution (std dev. 20%), and α_{EB} and $C_{\mathrm{f,JON}}$ with lognormal distributions (std dev. 50% and 80% respectively). The latter values reflect the greater uncertainty in the settings of these latter parameters, and the lognormal distributions were applied to prevent negative values.

[60] The combined calibration yielded the following parameter values: $B = 0.96$, $\alpha_{\mathrm{EB}} = 0.10$ (with $f_{\mathrm{max,EB}} = 2.5\, f_{\mathrm{m01}}$) and $C_{\mathrm{f,JON}} = 0.038\ \mathrm{m^2/s^3}$. Note that the latter setting agrees with that suggested previously by *Zijlema et al.* [2012]. These parameter settings, together with their corresponding source term expressions, constitute the model proposed here (labeled version 40.72ABCDE), which was used in the assessment of the Dutch primary sea defenses. Table 8 compares this model version to the default model described in section 3.2.

6. Validation of Proposed Model

[61] The calibrated model (as defined in Table 8) is subsequently evaluated for the total validation subset, as well as for each of the model innovations discussed in section 4.

Table 8. Comparison of the Settings of the Default SWAN Model and the Proposed Model, After Calibration

Source Term/Process	Default	Proposed
Wind input and whitecapping	*van der Westhuysen* [2007]	″
Quadruplet interaction	*Hasselmann et al.* [1985], $C_{nl4} = 3 \times 10^7$, $\lambda = 0.25$	″
Bottom friction	*Hasselmann et al.* [1973], $C_{f,JON} = 0.067$ m^2/s^3	*Hasselmann et al.* [1973], $C_{f,JON} = 0.038$ m^2/s^3
Depth-induced breaking	*Battjes and Janssen* [1978], $\alpha_{BJ} = 1.0$, $\gamma = 0.73$	*van der Westhuysen* [2009], $B = 0.96$, $\beta_{ref} = -1.396$, $\nu = 500$
Triad interaction	*Eldeberky* [1996], $\alpha_{EB} = 0.10$, $f_{max,EB} = 5\, f_{m01}$	*Eldeberky* [1996], $\alpha_{EB} = 0.10$, $f_{max,EB} = 2.5\, f_{m01}$
Enhanced current-induced dissipation	-	*van der Westhuysen* [2012], $C''_{ds} = 0.80$
Number of stationary iterations	80	″

[62] Figure 11 presents scatterplots of the hindcast results of all 161 data points in the validation subset for the default model variant described in section 3.2. The left-hand column shows that the default SWAN model (version 40.51) performs quite well, with most of the model-data points being around the line of perfect agreement. However, a negative relative bias can be seen for all parameters. Specifically, the data points trend away from the unity line for

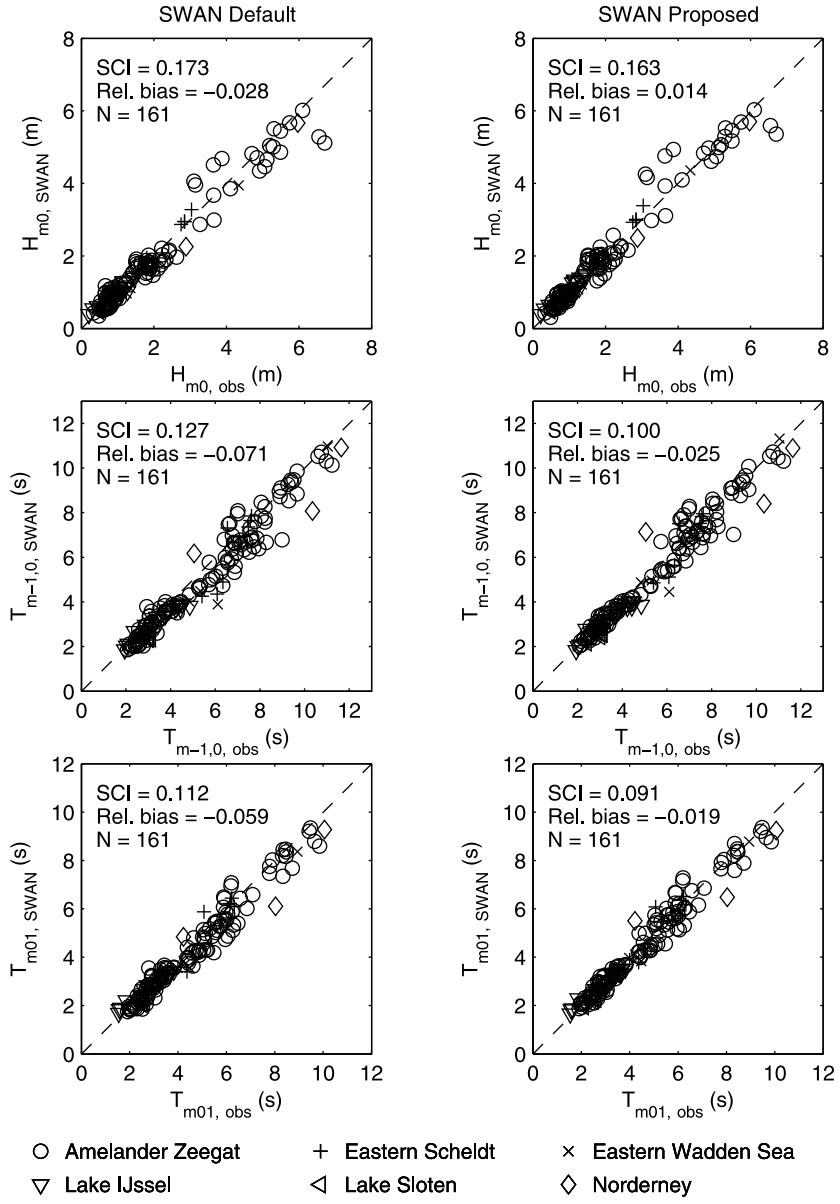

Figure 11. Scatterplots of model results versus observations, for all cases and locations in the validation subset. Shown are (top) significant wave height H_{m0} and spectral wave periods (middle) $T_{m-1,0}$ and (bottom) T_{m01}, for (left) the default model and (right) the proposed model. Integral parameters of model results calculated over the same frequency interval as available in the observations, which varies from site to site.

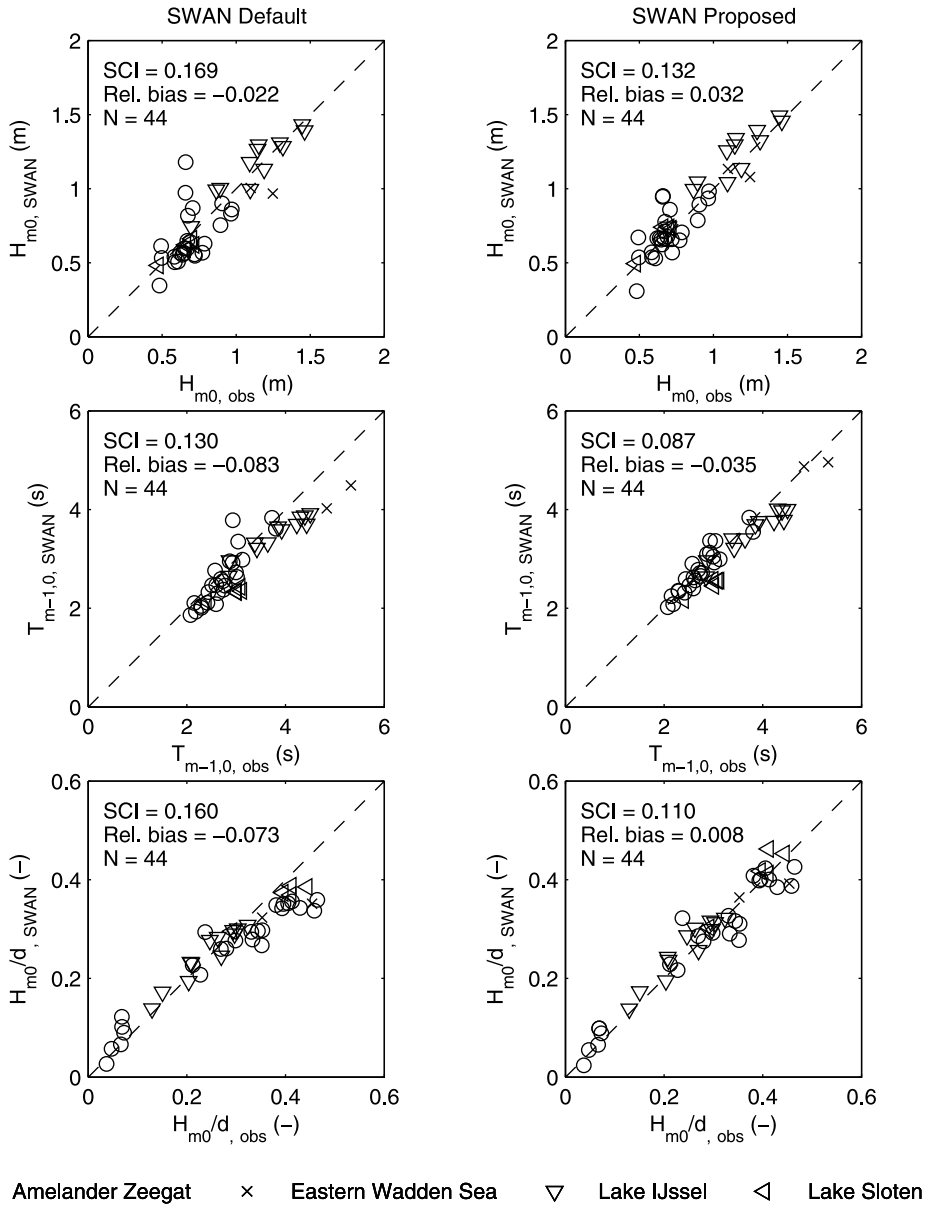

Figure 12. Scatterplots of model results versus observations for validation cases of finite-depth wave growth. Shown are the significant wave height, spectral wave period $T_{m-1,0}$ and the ratio H_{m0}/d for (left) the default model and (right) the proposed model.

larger values of wave height and period. Both aspects are of concern, since this means that SWAN in its default form would already underestimate nearshore wave conditions for these measured storm events, let alone normative events. Note that the default model results for the Norderneyer Seegat include current field input and the higher number of iterations discussed in section 4.2. The right-hand column of Figure 11 shows the scatterplot results of the proposed model as calibrated above. The right-hand column shows that the proposed model consistently reduces the bias obtained with the default model (left-hand column), and results in a smaller scatter index for all these parameters. For the stations in the Wadden Sea interior (e.g., AZB51, AZB61 and AZB62, deployment 2007–present) and in the shallow lakes (e.g., Lake Sloten), the improvement is mostly due to the formulation for depth-induced breaking of *van der Westhuysen* [2009] under finite-depth wave growth conditions, and the reduction of the constant bottom friction coefficient (discussed in sections 4.1 and 4.3 respectively).

[63] Figure 12 illustrates the improvement in model performance for finite-depth wave growth. The left-hand panels show the model results (validation subset) for the buoys AZB51, AZB61 and AZB62 landward of the Amelander Zeegat, and UHW1 and WRW1 in the Eastern Wadden Sea. These display an underestimation for the mean period $T_{m-1,0}$ and the ratio H_{m0}/d, which increases with increasing values of these variables. The default H_{m0}/d result displays an upper limit of about 0.38. By contrast, observed H_{m0}/d

ratios in the Dutch Wadden Sea flat areas reach values of up to 0.47. The H_{m0}/d ratios are consistent with observations from the shallow Lake IJssel and Lake Sloten [*Bottema and van Vledder*, 2009] included in Figure 12. The right-hand panels of Figure 12 show the results of the proposed model with respect to finite-depth wave growth and the proposed breaker model. The scatter index scores of all considered parameters improve compared to those of the default model. The bias likewise improves for $T_{m-1,0}$ and H_{m0}/d, but for H_{m0} it goes from a small negative bias to a small positive bias. Large improvements in the scatter index and bias can be seen for the H_{m0}/d ratio (bottom right). The apparent upper limit in the modeled H_{m0}/d values, seen in the bottom left-hand panel, virtually disappears when the breaker model of *van der Westhuysen* [2009] is applied. The relative bias reduces strongly, and the scatter to a lesser extent.

[64] Figure 5 shows that the wave spectra in the Amelander Zeegat produced using the proposed model are more energetic and represent a large improvement over those of the default model, especially at AZB51 an AZB61 (compare thick solid with dash-dotted relative to the data). The modeled wave directions are unchanged over the ranges of significant variance density. The largest remaining difference in variance density with the observations can be seen at AZB62. This is mainly due to the enhanced dissipation on current gradients—compare the proposed model result (thick solid) and the proposed model, but with $C''_{ds} = 0$ (solid with crosses). The enhanced dissipation tends to reduce the variance around the peak of the spectrum, tending away from the measurements in this case. This is due to the modeled strong current gradients at this location: the (wind-induced) northeasterly current has a value of about 0.8 m/s just upwind from AZB62 and near zero downwind due to the tidal channel, i.e., a negative gradient in a following current. As current field observations were not made in the Amelander Zeegat, we can not verify whether such a gradient occurred in nature.

[65] Figure 7 shows the results of the proposed model for the Norderneyer Seegat inlet case. The proposed model (thick solid lines) performs well at the RIFFGAT and VST1 stations, correcting the moderate overestimation of the default model (with currents, dash-dotted line) at the former location. However, the proposed model results are at a greater variance with the observations at SGTNEY, especially over frequencies <0.1 Hz arriving from offshore.

[66] Figure 8 shows the wave spectra results of the proposed model for two validation cases featuring wave-current interaction in the Amelander Zeegat channel. In the opposing current case (top panels), application of the expression for enhanced current-induced dissipation improves the prediction, although at buoy AZB42 the position of the peak frequency is not predicted well (compare thick solid with dash-dotted line). In the following current case, the proposed model shows a reduction in variance relative to the default at AZB42, improving the agreement with the measurements at AZB42. At AZB32, an increase relative to the default model results are found over the low-frequency peak, again improving agreement with the observations somewhat. This is due to a reduction in the level of depth-induced breaking dissipation of NW waves over the ebb tidal delta with the *van der Westhuysen* [2009] expression. These channel locations were found to be insensitive to the change in bottom friction from $C_{f,JON} = 0.067$ m^2/s^3 to 0.038 m^2/s^3 in the proposed model (not shown). The results for wave direction are essentially unchanged relative to those of the default model, still showing differences with the observations only at AZB42. Here both model variants predict waves from the WNW whereas they are observed from the WSW. Clearly the proposed model's predictions do not match the data in this case, which leaves room for further improvement.

[67] Figure 9 shows the results of the proposed model (thick line) with respect to wave penetration. With the reduction in bottom friction dissipation, the variance in the low-frequency flank of the spectra at the Eastern Wadden Sea's nearshore buoys is increased relative to the default (compare with results for the proposed model, but with $C_{f,JON} = 0.067$ m^2/s^3, dashed). However, the proposed model results still fall short of the measurements, except at WRW1. Figure 13 compares the model results with observations in terms of scatterplots for locations where low-frequency wave penetration is significant. The left-hand column shows the results of the default model, where a clear underprediction in H_{m0}, $T_{m-1,0}$ and T_{m01} is observed. The right-hand column of Figure 13 shows that using the proposed model (including the lower bottom friction) leads to a significant improvement in the statistics of the wave parameters: the bias is halved and the scatter greatly reduced. These results are consistent with independently obtained results of *Zijlema* [2009].

[68] To investigate the influence of the bottom friction on these results, the proposed SWAN version without the reduction of the bottom friction (therefore $C_{f,JON} = 0.067$ m^2/s^3) is compared to the proposed model itself (Figure 13, middle and right-hand columns, respectively). The center column shows wave parameter results that lie in between the underpredicted values of the default model and those of the proposed model. It can therefore be concluded that the improved results at the lower frequencies and at the stations where wave penetration is relevant are in part due to the reduction of the bottom friction (judging from the reduction in the bias by about 50%) and in part due to the other model changes discussed above.

[69] Summarizing, it can be concluded from these results that the proposed model innovations have led to improved overall performance in the complex tidal inland field situations considered in this study.

7. Discussion

[70] A number of innovations have been proposed here to improve the nearshore wind-wave model SWAN for application to complex tidal inlet regions. However, there are still a number of remaining challenges and information needs for wave modeling in these regions, and some reservations should be borne in mind when applying the results of this study.

[71] First, the present effort focused on the Wadden Sea, the Eastern Scheldt and a collection of shallow Dutch lakes. Whereas a wide range of conditions is considered here, the

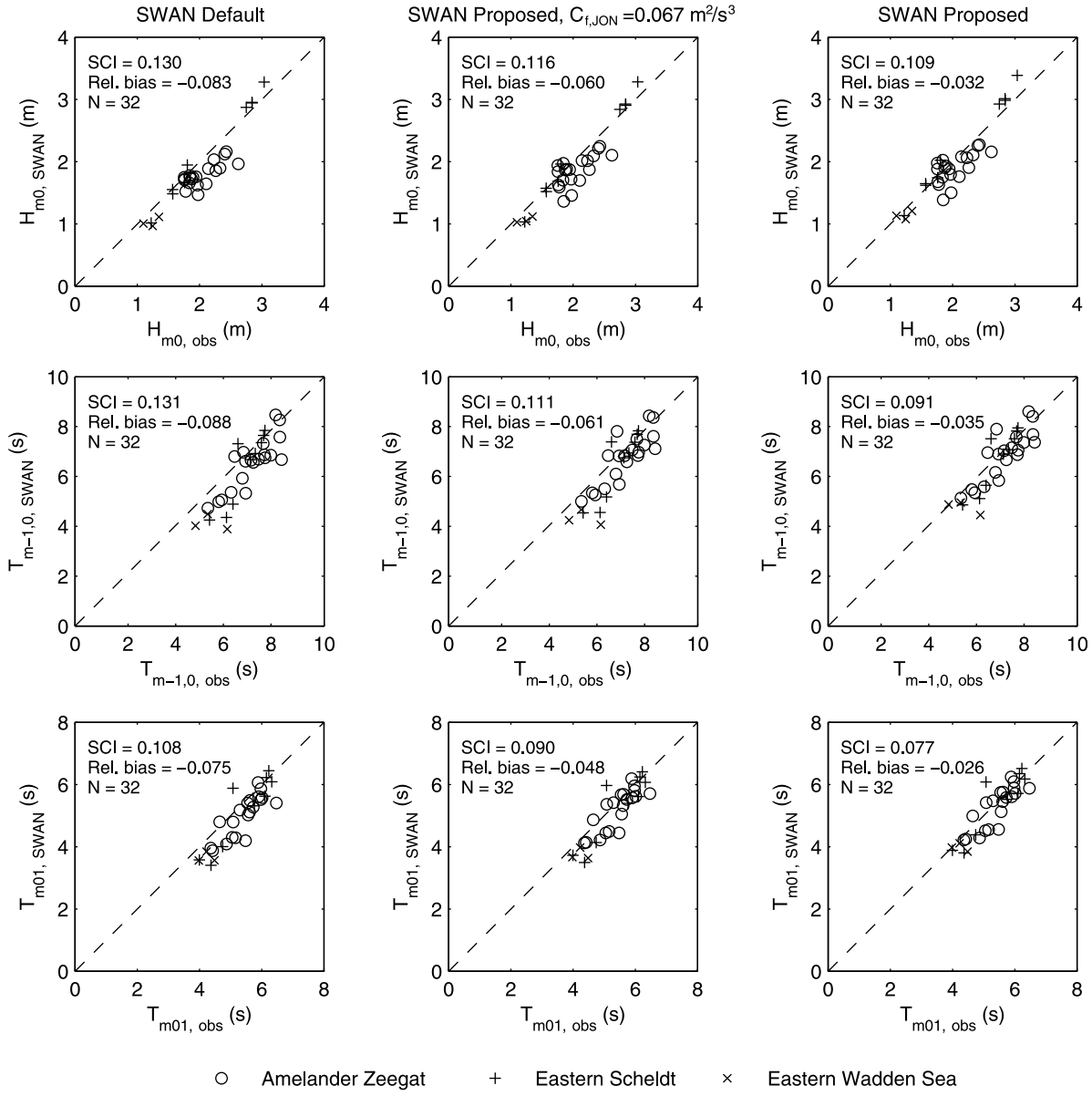

Figure 13. Scatterplots of model results versus observations for validation cases of North Sea wave penetration. Shown are (top) significant wave height H_{m0} and mean wave periods (middle) $T_{m-1,0}$ and (bottom) T_{m01}, for the buoys AZB21 and AZB22 in the Amelander Zeegat, BG2, DORA and OS4 in the Eastern Scheldt and PBW1, UHW1 and WRW1 in the Eastern Wadden Sea. Left column: default model. Middle column: proposed model with $C_{f,JON}$ = 0.067 m^2/s^3. Right column: proposed model.

applicability of the proposed model formulation and settings should be verified for other tidal inlet systems as well.

[72] A number of modeling challenges remain for tidal inlet areas such as the Wadden Sea. Wave propagation patterns in the Wadden Sea should be studied further, and more extensively, using, e.g., X-band radar, or High Frequency (HF) radar and Synthetic Aperture Radar (SAR) for greater range. Propagation modeling in complex domains such as the Wadden Sea should be investigated further, including comparing the results of the linear, phase-averaged model SWAN to nonlinear phase-resolving models.

[73] The second aspect of modeling low-frequency wave penetration is the associated dissipation. Analysis of spectral evolution (section 4.3) suggested bottom friction to be the most important dissipation mechanism over the extensive tidal flats. The re-analysis of *Zijlema et al.* [2012] lends support to the use of a lower constant bottom friction coefficient in the *Hasselmann et al.* [1973] bottom friction formulation for the Wadden Sea interior. However, a more fundamental investigation of this issue is possible, using dynamic bed ripple modeling [e.g., *Tolman*, 1994]. Such a

dynamic bed ripple formulation has recently been implemented in SWAN [*Smith et al.*, 2011].

[74] Regarding the enhanced dissipation of waves on negative current gradients (section 4.2), it was noted that such gradients can occur in both accelerating (along the wave's propagation path) opposing current and decelerating following current. The former has been observed in a number of field and laboratory experiments. To our knowledge, the flume setup of *Babanin et al.* [2011] is the only experiment that features a negative current gradient in following current. Their results indeed show that waves steepen on a decelerating following current, which can lead to breaking dissipation. More observations of this situation would be a very useful addition to the subject of wave-current interaction modeling.

[75] This paper does not discuss the accuracy of the input fields into SWAN, such as wind fields, bathymetry, and water level and current fields. Wind fields applied here were mostly obtained from HIRLAM, which is a state-of-the-art wind- and pressure field model. Still, differences between the computed wind fields and local observations are present, and could explain some of the inaccuracies in the wave model results. The bathymetry of the tidal inlet seas is measured during the summer months with intervals ranging from 1 to 4 years because of the expense of measurement campaigns. This is not ideal, because bathymetry data from different years had to be assembled, and the inlet bathymetry is highly dynamic on timescales of months (summer to winter) and years. The current and water level fields have been computed with the hydrodynamic models Delft3D and WAQUA. These models are calibrated against observations of water levels from local water level gauges (Figure 1). We have found that the surge peak was consistently underestimated (sometimes up to 0.40 m) by the hydrodynamic models, the reason of which is still under investigation. For the present purpose, the water levels used as input in the SWAN calculations were corrected for the discrepancies using linear interpolation between observation stations. Current fields were adjusted accordingly by applying continuity locally. Furthermore, even if the hydrodynamic models showed perfect skill with regard to the water level data, this does not guarantee that the modeled currents are modeled correctly. For this purpose, 3D current measurements are required in the tidal channels and, to capture the influence on the young wind sea, also on the tidal flats.

[76] Finally, it should be noted that even though the observations in the Dutch Wadden Sea and elsewhere presented here include some significant events over the observation period, they still represent only relatively mild storm conditions compared to the extreme events applicable to design and testing which will probably not be measured in our lifetime. The step from measured to normative conditions makes an implicit assumption about the scalability of the applied physics.

8. Conclusions

[77] This study presents the main results of a five-year research program to assess and where possible improve the performance of the wave transformation model SWAN in the Dutch Wadden Sea, with a focus on the shallow water processes. A number of model innovations have been developed, and were sequentially jointly calibrated and compared to the default model results. The assessment was done on the basis of extensive wave measurements conducted in the Amelander Zeegat tidal inlet and the Eastern Dutch Wadden Sea, as well as relevant data from lakes, estuaries and beaches. On the basis of these results, the following can be concluded:

[78] 1. SWAN version 40.51, in its default form of 2006 (except for wind input and whitecapping modeled according to *van der Westhuysen* [2007]) was found to perform reasonably well for storm conditions. However, three aspects required further attention: (i) the modeling of depth-induced breaking under finite-depth wave growth conditions, (ii) the modeling of wave-current interaction, and (iii) the penetration of low-frequency wind waves.

[79] 2. Over the tidal flats, the computed ratio of significant wave height over water depth showed an apparent upper limit using the default version of SWAN, underestimating observations. This is because the wave growth over finite depth is hampered by the *Battjes and Janssen* [1978] formulation of depth-induced wave breaking using a fixed breaker parameter γ, calibrated for sloping bed surf zones. The problem has been solved using a new breaker formulation of *van der Westhuysen* [2009, 2010], which depends on local wave characteristics.

[80] 3. Additional dissipation was required to reduce overprediction of the significant wave height in negative current gradients (opposing and following current) in the tidal channels. This has largely been achieved with a formulation for enhanced dissipation that is scaled with the degree of Doppler-induced steepening of the waves. Note, however, that the limited size of the data set for following current prevents the drawing of a definitive conclusion.

[81] 4. Currents should be included in the computations as they affect the wave age, which has consequences for the modeled variance spectra. In many (but not all) locations considered here this inclusion improved the model results.

[82] 5. The primary spectral peak of North Sea waves penetrating into the inlet was underpredicted, with inaccurate modeling of propagation and dissipation (bottom friction) being the likely causes. On the basis of comparisons with X-band radar derived results, the propagation aspect appears to be adequately modeled in the inlet gorge, but this has not been verified deeper into the Wadden Sea. Model improvement was found when the bottom friction coefficient was recalibrated to $C_{f,JON} = 0.038\ m^2/s^3$, which is consistent with a re-analysis by *Zijlema et al.* [2012].

[83] 6. As demonstrated in the simulations for the Norderneyer Seegat, wave computations should be performed using a sufficient number of iterations to ensure convergence. This confirms the findings of *Zijlema and van der Westhuysen* [2005]. In the present study 80 iterations were found to be sufficient.

[84] All these improvements have resulted in a relative bias reduction in H_{m0} from -3% to -1%, in $T_{m-1,0}$ from -7% to -3%, and in T_{m01} from -6% to -2%, and consistent reductions in scatter, compared to the 2006 default model (Figure 11). The resulting statistical error parameters are considered small enough for the proposed model to be

used to determine reliable normative wave conditions in the Dutch Wadden Sea.

Appendix A

[85] This appendix provides details of the source term formulations in SWAN that were modified or calibrated in this study.

A1. Whitecapping Dissipation

[86] The expression applied for whitecapping dissipation is by *van der Westhuysen* [2007]. It is an adapted version of the saturation-based formulation of *Alves and Banner* [2003], and is combined with the wind input expression of *Yan* [1987]. The whitecapping expression is composed of two parts, namely a contribution to the dissipation by wave breaking, and a weaker non-breaking contribution:

$$S_{\mathrm{wc}}(\sigma,\theta) = f_{\mathrm{br}}(\sigma) S_{\mathrm{dis,break}} + [1 - f_{\mathrm{br}}(\sigma)] S_{\mathrm{dis,non-break}}, \qquad \text{(A1)}$$

where the breaking part is based on the saturation-based expression of *Alves and Banner* [2003], as modified by *van der Westhuysen et al.* [2007]:

$$S_{\mathrm{dis,break}} = -C'_{\mathrm{ds}} \left[\frac{B(k)}{B_{\mathrm{r}}}\right]^{\frac{p}{2}} [\tanh(kd)]^{\frac{2-p}{4}} g^{\frac{1}{2}} k^{\frac{1}{2}} E(\sigma,\theta), \qquad \text{(A2)}$$

where k is the wave number and g gravitational acceleration. The non-breaking part is based on the pulse-based expression of *Komen et al.* [1984]:

$$S_{\mathrm{dis,non-break}} = -C_{\mathrm{ds}} \left(\frac{k}{\tilde{k}}\right)^{q} \left(\frac{\tilde{s}}{\tilde{s}_{\mathrm{PM}}}\right)^{r} \tilde{\sigma} E(\sigma,\theta). \qquad \text{(A3)}$$

[87] The weighting factor f_{br} determines the changeover from the dissipation of breaking to non-breaking waves. This weighting is a function of the ratio between the spectral saturation $B(k)$ and a threshold saturation level B_{r}:

$$f_{\mathrm{br}}(\sigma) = \frac{1}{2} + \frac{1}{2} \tanh\left\langle 10 \left(\left[\frac{B(k)}{B_{\mathrm{r}}}\right]^{\frac{1}{2}} - 1 \right) \right\rangle. \qquad \text{(A4)}$$

Here $\tilde{k}$ is the mean wavenumber (see definition below), $\tilde{\sigma}$ the mean radian frequency, $\tilde{s} = \tilde{k}\sqrt{E_{\mathrm{tot}}}$ the mean wave steepness and $\tilde{s}_{\mathrm{PM}}$ the mean steepness of the *Pierson and Moskowitz* [1964] spectrum. The tuning parameters are set to $C_{\mathrm{ds}} = 2.36 \times 10^{-5}$, $q = 1$ and $r = 4$.

[88] For the spatial scales considered in the field cases of the present study, only the component (A2) in the expression (A1) is relevant. The parameter p in (A2) is a function of the inverse wave age u_*/c, based on scaling arguments involving a spectral balance between the wind input, whitecapping and nonlinear interaction terms (see *van der Westhuysen et al.* [2007] for details):

$$p\left(u_*/c\right) = 3 + \tanh\left[25\left(\frac{u_*}{c} - 0.1\right)\right]. \qquad \text{(A5)}$$

[89] In *van der Westhuysen* [2007], the remaining parameters of (A2) were calibrated to $C'_{\mathrm{ds}} = 5.0 \times 10^{-5}$ and $B_{\mathrm{r}} = 1.75 \times 10^{-3}$ respectively.

A2. Depth-Induced Breaking

[90] Depth-induced breaking is computed according to the biphase breaker model of *van der Westhuysen* [2009, 2010]:

$$D_{\mathrm{tot}} = -\frac{3\sqrt{\pi}}{16} \frac{B^3 \tilde{f}}{d} \left(\frac{\beta}{\beta_{\mathrm{ref}}}\right)^{n} H_{\mathrm{rms}}^3, \qquad \text{(A6)}$$

in which B is a proportionality coefficient, $\tilde{f}$ the mean frequency, H_{rms} the root-mean square wave height, and β the biphase of the self-interactions of the peak frequency components, parameterized by *Eldeberky* [1996] as:

$$\beta = -\frac{\pi}{2} + \frac{\pi}{2} \tanh\left(\frac{0.2}{Ur}\right), \qquad \text{(A7)}$$

with

$$Ur = \frac{g}{8\sqrt{2}\pi^2} \frac{H_{\mathrm{m0}} T_{\mathrm{m01}}^2}{d^2}, \qquad \text{(A8)}$$

in which Ur is the Ursell number, T_{m01} the mean period, and β_{ref} the reference biphase at which all waves are breaking. The exponent n relates the biphase to the fraction of breaking waves. *Van der Westhuysen* [2009] shows this relation to be dependent on the local mean steepness:

$$n = \frac{n_1 + n_2}{2} - \frac{n_2 - n_1}{\pi} \arctan\left[\nu\left(S_{\mathrm{loc}} - \tilde{S}_{\mathrm{loc}}\right)\right] \qquad \text{(A9)}$$

where $n_1 = 2$, $n_2 = 6$ and ν are shape factors. The local mean steepness S_{loc} is given by:

$$S_{\mathrm{loc}} = \frac{H_{\mathrm{rms}} \tilde{k}}{2\pi}, \quad \tilde{k} = \left[\frac{\iint k^{-\frac{1}{2}} E(\sigma,\theta) d\sigma d\theta}{E_{\mathrm{tot}}}\right]^{-2}, \qquad \text{(A10)}$$

with an average value of $\tilde{S}_{\mathrm{loc}}$. The source term is compiled from (A6) assuming the dissipation per spectral component to be proportional to its variance density, after *Battjes and Beji* [1992]:

$$S_{\mathrm{brk}}(\sigma,\theta) = D_{\mathrm{tot}} \frac{E(\sigma,\theta)}{E_{\mathrm{tot}}}, \qquad \text{(A11)}$$

where E_{tot} is the total variance. The biphase breaker model (A6)–(A11) contains a total of four calibration parameters, namely the proportionality coefficient B, the reference biphase β_{ref}, the shape factor ν and the average steepness $\tilde{S}_{\mathrm{loc}}$. *Van der Westhuysen* [2009] determined the latter three parameters at $\beta_{\mathrm{ref}} = -4\pi/9 = -1.396$ and $\nu = 500$ and $\tilde{S}_{\mathrm{loc}} = 0.038$ from the data of *Boers* [1996]. The calibration of the parameter B is considered in section 5 in the main text.

A3. Enhanced Current-Induced Whitecapping

[91] Enhanced wave dissipation in the presence of negative current gradients is modeled using the expression of *van der Westhuysen* [2012], which is based on the saturation-based whitecapping formulation of *van der Westhuysen et al.* [2007]. In order to isolate the contribution of currents in the increased steepness and resulting dissipation, the degree of dissipation in this expression is scaled with the incremental shortening/steepening of the waves due to

negative current gradients, which is related to the relative Doppler shifting rate c_σ/σ. In this way, the generation of young wind seas is not suppressed. The formulation reads:

$$S_{\mathrm{wc,cur}}(\sigma,\theta) = -C''_{\mathrm{ds}} \max\left[\frac{c_\sigma(\sigma,\theta)}{\sigma}, 0\right]\left[\frac{B(k)}{B_{\mathrm{r}}}\right]^{\frac{p}{2}} E(\sigma,\theta), \quad \text{(A12)}$$

where the propagation in sigma space c_σ is given by [e.g., *Mei*, 1983]:

$$\frac{d\sigma}{dt} = c_\sigma = \frac{\partial\sigma}{\partial d}\left[\frac{\partial d}{\partial t} + \vec{U}\cdot\nabla d\right] - c_{\mathrm{g}}\vec{k}\cdot\frac{\partial\vec{U}}{\partial s}, \quad \text{(A13)}$$

in which s is the space coordinate in the propagation direction θ. A maximum function is included in (A12) in order to take only relative increases in steepness into account in the enhanced dissipation. Note that negative current gradients occur both for accelerating opposing currents and decelerating following currents, both of which result in steepening of the waves. The terms on the RHS of (A13) vary with the local conditions. However, considering the large relative depth in the tidal channels and the alignment of the current with the channel walls, the last term is considered to be dominant in the cases considered here (J. A. Battjes, personal communication, July 2011). Expression (A12) contains one additional calibration parameter, namely the proportionality coefficient C''_{ds}, the value of which is discussed in the main text. The remaining parameters are as defined and calibrated in *van der Westhuysen et al.* [2007]; see Appendix A1.

A4. Bottom Friction

[92] The bottom friction expression applied in this study is the JONSWAP empirical model of *Hasselmann et al.* [1973]. It is given by:

$$S_{\mathrm{bot}}(\sigma,\theta) = -C_{\mathrm{f,JON}}\frac{\sigma^2}{g^2\sinh^2(kd)}E(\sigma,\theta). \quad \text{(A14)}$$

[93] The calibration of the proportionality coefficient $C_{\mathrm{f,JON}}$ for local conditions is considered in section 5 in the main text.

A5. Triad Nonlinear Wave Interaction

[94] The default expression for nonlinear triad wave interactions in SWAN is the LTA of *Eldeberky* [1996]:

$$S_{\mathrm{nl3}}(\sigma,\theta) = S^{-}_{\mathrm{nl3}}(\sigma,\theta) + S^{+}_{\mathrm{nl3}}(\sigma,\theta) \quad \text{(A15)}$$

with

$$S^{+}_{\mathrm{nl3}}(\sigma,\theta) = \max\left[0, \alpha_{\mathrm{EB}}2\pi c c_g J^2 |\sin\beta|\left\{E^2(\sigma/2,\theta) - 2E(\sigma/2,\theta)E(\sigma,\theta)\right\}\right] \quad \text{(A16)}$$

and

$$S^{-}_{\mathrm{nl3}}(\sigma,\theta) = -2S^{+}_{\mathrm{nl3}}(2\sigma,\theta). \quad \text{(A17)}$$

[95] The LTA formulation was implemented in SWAN along each propagation direction of the directional spectrum, yielding an isotropic, directionally decoupled representation of triad interaction. Triad interaction modeled by the LTA includes only collinear self sum interactions, for one-dimensional spectral evolution. Since only sum interaction is considered, only superharmonics are created. Furthermore, since only self interactions are included, only the first ($2\sigma_p$), third ($4\sigma_p$), etc. superharmonics of the spectral peak are reproduced. Since the biphase β is parameterized without phase information, nonlinear transfer of energy in the model occurs only in one direction through the spectrum. This excludes the phenomenon of recurrence (reversal of energy transfer back to the spectral peak), which is observed over the inshore slope of submerged bars, for example. The interaction coefficient J, describing self interaction in the nonlinearity range $0 \le Ur \le 1$, is given by *Madsen and Sørensen* [1993]:

$$J = \frac{k^2_{\sigma/2}\left(gd + 2c^2_{\sigma/2}\right)}{k_\sigma d\left(gd + \frac{2}{15}gd^3k^2_\sigma - \frac{2}{5}\sigma^2d^2\right)}. \quad \text{(A18)}$$

[96] The default value of the proportionality coefficient of the LTA in SWAN 40.51 is $\alpha_{\mathrm{EB}} = 0.10$. Recalibration of α_{EB} is considered in the combined calibration described in section 5 in the main text. The results produced by the LTA are also quite sensitive to the choice of the frequency up to which the interactions are calculated, denoted here as $f_{\mathrm{max,EB}}$. SWAN 40.51 features a setting of $f_{\mathrm{max,EB}} = 5\ f_{\mathrm{m01}}$. In the present calibration, this has been changed to $f_{\mathrm{max,EB}} = 2.5\, f_{m01}$ based on *Ris* [1997].

[97] **Acknowledgments.** This study is part of the SBW (Strength and Loads on Water Defenses) project commissioned by Rijkswaterstaat Centre for Water Management in the Netherlands. The lead partner is Deltares in collaboration with Rijkswaterstaat's Data Division (DID) who collected data, and with researchers from universities and Dutch consultants Alkyon/Arcadis, Royal Haskoning, Svašek Hydraulics, Witteveen+Bos and SeaDarQ to perform hindcasts and analyze the results. Thanks are due to the Deltares OpenDA team, in particular Martin Verlaan, Stef Hummel and Henk van den Boogaard. Ralph Kaiser and Hanz Niemeyer are thanked for providing the Norderney data. Sepehr Eslami Arab is thanked for his assistance in producing figures.

References

Alves, J. H. G. M., and M. L. Banner (2003), Performance of a saturation-based dissipation-rate source term in modelling the fetch-limited evolution of wind waves, *J. Phys. Oceanogr.*, *33*, 1274–1298.

Apotsos, A., B. Raubenheimer, S. Elgar, and R. T. Guza (2008), Testing and calibrating parametric wave transformation models on natural beaches, *Coastal Eng.*, *55*, 224–235.

Babanin, A. V., H.-H. Hwung, I. Shugan, A. Roland, A. J. van der Westhuysen, A. Chawla, and C. Gautier (2011), Nonlinear waves on collinear currents with horizontal velocity gradient, paper presented at 12th International Workshop on Wave Hindcasting and Forecasting, Environ. Can., Kohala Coast, Hawaii. [Available at http://www.waveworkshop.org/12thWaves.]

Battjes, J. A., and S. Beji (1992), Breaking waves propagating over a shoal, in *Proceedings of the 23rd International Conference on Coastal Engineering, Venice, Italy, 1992*, pp. 42–50, Am. Soc. of Civ. Eng., Reston, Va.

Battjes, J. A., and J. P. F. M. Janssen (1978), Energy loss and set-up due to breaking of random waves, in *Proceedings of the 16th International Conference on Coastal Engineering, Hamburg, Germany, 1978*, pp. 569–588, Am. Soc. of Civ. Eng., Reston, Va.

Battjes, J. A., and M. J. F. Stive (1985), Calibration and verification of a dissipation model for random breaking waves, *J. Geophys. Res.*, *90*(C5), 9159–9167.

Birkemeier, W. A., C. Donoghue, C. E. Long, K. K. Hathaway, and C. F. Baron (1997), 1990 DELILAH nearshore experiment: Summary Report, *Tech. Rep. CHL-97-24*, 213 pp., Waterw. Exp. Stn., U.S. Army Corps of Eng., Vicksburg, Miss.

Boers, M. (1996), Simulation of a surf zone with a barred beach; Report 1: Wave heights and wave breaking, technical report, Fac. of Civ. Eng., Delft Univ. of Technol., Delft, Netherlands. [Available at http://repository.tudelft.nl.]

Booij, N., R. C. Ris, and L. H. Holthuijsen (1999), A third generation wave model for coastal regions: 1. Model description and validation, *J. Geophys. Res.*, *104*(C4), 7649–7666.

Bottema, M., and G. P. van Vledder (2009), A ten-year data set for fetch- and depth-limited wave growth, *Coastal Eng.*, *56*, 703–725.

Bouws, E., and G. J. Komen (1983), On the balance between growth and dissipation in an extreme, depth-limited wind-sea in the southern North Sea, *J. Phys. Oceanogr.*, *13*(9), 1653–1658.

De Waal, J. P. (2001), Wave growth limit in shallow water, in *Ocean Wave Measurement and Analysis*, pp. 560–569, Am. Soc. of Civ. Eng., Reston, Va.

De Waal, J. P., D. Beyer, J. H. Andorka Gal, L. H. Holthuijsen, G. P. van Vledder, J. P. F. M. Janssen, and D. P. Hurdle (1997), Instellingen golfmodel HISWA, toe te passen bij productiesommen in het IJsselmeergebied [Model settings of the wave model HISWA, to be used in production runs for Lake IJssel], *Werkdoc. 97.183X*, RWS RIZA, Rotterdam, Netherlands.

Doering, J. C., and A. J. Bowen (1995), Parametrization of orbital velocity asymmetries of shoaling and breaking waves using bispectral analysis, *Coastal Eng.*, *26*(1–2), 15–33.

Eldeberky, Y. (1996), Nonlinear transformations of wave spectra in the nearshore zone, PhD thesis, Fac. of Civ. Eng., 203 pp., Delft Univ. of Technol., Delft, Netherlands. [Available at http://repository.tudelft.nl.]

Hasselmann, K. (1962), On the non-linear energy transfer in a gravity-wave spectrum: I. General theory, *J. Fluid Mech.*, *12*, 481–500.

Hasselmann, K., et al. (1973), Measurement of wind-wave growth and swell decay during the Joint North Sea Wave Project (JONSWAP), *Dtsch. Hydrogr. Z., A*, *8*(12), suppl., 95 pp.

Hasselmann, S., K. Hasselmann, J. A. Allender, and T. P. Barnett (1985), Computations and parameterizations of the nonlinear energy transfer in a gravity-wave spectrum. Part 2: Parameterization of the nonlinear transfer for application in wave models, *J. Phys. Oceanogr.*, *15*, 1378–1391.

Haus, B. K. (2007), Surface current effects on the fetch-limited growth of wave energy, *J. Geophys. Res.*, *112*, C03003, doi:10.1029/2006JC003924.

Herbers, T. H. C., S. Elgar, and R. T. Guza (1994), Infragravity-frequency (0.005–0.05 Hz) motions on the shelf: I. Forced waves, *J. Phys. Oceanogr.*, *24*, 917–927.

Herbers, T. H. C., and M. C. Burton (1997), Nonlinear shoaling of directionally spread waves on a beach, *J. Geophys. Res.*, *102*, 21,101–21,114.

Herbers, T. H. C., N. R. Russnogle, and S. Elgar (2000), Spectral energy balance of breaking waves within the surf zone, *J. Phys. Oceanogr.*, *30*, 2723–2737.

Herman, A., R. Kaiser, and H. D. Niemeyer (2006), Medium-term wave and current modeling for a mesotidal Wadden Sea coast, in *Proceedings of the 30th International Conference on Coastal Engineering, San Diego, USA, 2006*, pp. 628–639, Am. Soc. of Civ. Eng., Reston, Va.

Holthuijsen, L. H., N. Booij, and T. H. C. Herbers (1989), A prediction model for stationary, short-crested waves in shallow water with ambient currents, *Coastal Eng.*, *13*, 23–54.

Kaiser, R., and H. D. Niemeyer (2001), Analysis of directional spectra in shallow environment, in *Ocean Wave Measurement and Analysis*, pp. 944–952, Am. Soc. of Civ. Eng., Reston, Va.

Komen, G. J., S. Hasselmann, and K. Hasselmann (1984), On the existence of a fully developed wind-sea spectrum, *J. Phys. Oceanogr.*, *14*, 1271–1285.

Madsen, P. A., and O. R. Sørensen (1993), Bound waves and triad interactions in shallow water, *J. Ocean Eng.*, *20*(4), 359–388.

Mei, C. C. (1983), *The Applied Dynamics of Ocean Surface Waves*, 740 pp., John Wiley, New York.

Nelson, R. C. (1994), Depth limited design wave heights in very flat regions, *Coastal Eng.*, *23*, 43–59.

Pierson, W. J., and L. Moskowitz (1964), A proposed spectral form for fully developed wind seas based on the similarity theory of S. A. Kitaigorodskii, *J. Geophys. Res.*, *69*(24), 5181–5190.

Ralston, M. L., and R. I. Jennrich (1978), DUD, a derivative-free algorithm for nonlinear least squares, *Technometrics*, *20*, 7–14.

Ris, R. C. (1997), Spectral modelling of wind waves in coastal waters, PhD thesis, 160 pp., Fac. of Civ. Eng., Delft Univ. of Technol., Delft, Netherlands. [Available at http://repository.tudelft.nl.]

Ris, R. C., and L. H. Holthuijsen (1996), Spectral modelling of current wave-blocking, in *Proceedings of the 25th International Conference on Coastal Engineering, Orlando, USA, 1996*, pp. 1247–1254, Am. Soc. of Civ. Eng., Reston, Va.

Ris, R. C., L. H. Holthuijsen, and N. Booij (1999), A third-generation wave model for coastal regions: 2. Verification, *J. Geophys. Res.*, *104*(C4), 7667–7681.

Ruessink, B. G., D. J. R. Walstra, and H. N. Southgate (2003), Calibration and verification of a parametric wave model on barred beaches, *Coastal Eng.*, *48*, 139–149.

Smith, G., A. V. Babanin, P. Riedel, I. R. Young, S. Oliver, and G. Hubbert (2011), Introduction of a new friction routine in the SWAN model that evaluates roughness due to bedform and sediment size changes, *Coastal Eng.*, *58*(4), 317–326.

Stelling, G. S. (1983), On the construction of computational methods for shallow water flow problems, PhD thesis, Delft Univ. of Technol., Delft, Netherlands. [Available at http://repository.tudelft.nl.]

Thornton, E. B., and R. T. Guza (1983), Transformation of wave height distribution, *J. Geophys. Res.*, *88*, 5925–5938.

Tolman, H. L. (1994), Wind waves and movable-bed bottom friction, *J. Phys. Oceanogr.*, *24*(5), 994–1009.

Undén, P., L. Rontu, H. Järvinen, P. Lynch, J. Calvo, and G. Cats (2002), HIRLAM-5 scientific documentation, 144 pp., HIRLAM-5 Proj., Swed. Meteorol. and Hydrol. Inst., Norrköping, Sweden.

van der Westhuysen, A. J. (2007), Advances in the spectral modelling of wind waves in the nearshore, PhD thesis, 207 pp., Fac. of Civ. Eng., Delft Univ. of Technol., Delft, Netherlands. [Available at http://repository.tudelft.nl.]

van der Westhuysen, A. J. (2009), Modelling of depth-induced wave breaking over sloping and horizontal beds, paper presented at 11th International Workshop on Wave Hindcasting and Forecasting, Environ. Can., Halifax, Nova Scotia, Canada. [Available at http://www.waveworkshop.org/11thWaves.]

van der Westhuysen, A. J. (2010), Modelling of depth-induced wave breaking under finite-depth wave growth conditions, *J. Geophys. Res.*, *115*, C01008, doi:10.1029/2009JC005433.

van der Westhuysen, A. J. (2012), Spectral modeling of wave dissipation on negative current gradients, *Coastal Eng.*, *68*, 17–30.

van der Westhuysen, A. J., M. Zijlema, and J. A. Battjes (2007), Nonlinear saturation based whitecapping dissipation in SWAN for deep and shallow water, *Coastal Eng.*, *54*, 151–170.

Weerts, A. H., G. Y. El Serafy, S. Hummel, J. Dhondia, and H. Gerritsen (2010), Application of generic data assimilation tools (DATools) for flood forecasting purposes, *Comput. GeoSci.*, *36*, 453–463.

Yan, L. (1987), An improved wind input source term for third generation ocean wave modeling, *Tech. Rep. 87-8*, R. Netherlands Meteorol. Inst., De Bilt, Netherlands.

Young, I. R., and A. V. Babanin (2006), The form of the asymptotic depth-limited wind wave frequency spectrum, *J. Geophys. Res.*, *111*, C06031, doi:10.1029/2005JC003398.

Young, I. R., and L. A. Verhagen (1996), The growth of fetch-limited waves in water of finite depth. Part 1. Total energy and peak frequency, *Coastal Eng.*, *29*, 47–78.

Zijderveld, A., and H. Peters (2008), Measurement programme Dutch Wadden Sea, in *Proceedings of the 31st International Conference on Coastal Engineering, Hamburg, Germany, 2008*, pp. 404–410, Am. Soc. of Civ. Eng., Reston, Va.

Zijlema, M. (2009), Multiscale simulations using unstructured mesh SWAN model for wave hindcasting in the Dutch Wadden Sea, in *Proceedings of Coastal Dynamics 2009*, edited by M. Mizuguchi and S. Sato, pp. 1–12, World Sci., Singapore.

Zijlema, M., and A. J. van der Westhuysen (2005), On convergence behaviour and numerical accuracy in stationary SWAN simulations of nearshore wind wave spectra, *Coastal Eng.*, *52*, 237–256.

Zijlema, M., G. P. van Vledder, and L. H. Holthuijsen (2012), Bottom friction and wind drag for wave models, *Coastal Eng.*, *65*, 19–26.